

The spectroscopic Hertzsprung-Russell diagram of hot massive stars in the SMC

N. CASTRO,¹ M. S. OHEY,¹ L. FOSSATI,² AND N. LANGER³

¹ University of Michigan, 311 West Hall, 1085 S. University Avenue, Ann Arbor, MI 48109-1107, USA

² Space Research Institute, Austrian Academy of Sciences, Schmiedlstrasse 6, 8042 Graz, Austria

³ Argelander-Institut für Astronomie, Universität Bonn, Auf dem Hügel 71, 53121 Bonn, Germany

(Accepted October 8, 2018)

Submitted to ApJ

ABSTRACT

We present a comprehensive stellar atmosphere analysis of 329 O- and B-type stars in the Small Magellanic Cloud (SMC) from the RIOTS4 survey. Using spectroscopically derived effective temperature (T_{eff}) and surface gravities, we find that classical Be stars appear misplaced to low T_{eff} and high luminosity in the spectroscopic Hertzsprung-Russell diagram (sHRD). Together with the most luminous stars in our sample, the stellar masses derived from the sHRD for these objects are systematically larger than those obtained from the conventional HRD. This suggests that the well-known, spectroscopic mass-discrepancy problem may be linked to the fact that both groups of stars have outer envelopes that are nearly gravitationally unbound. The non-emission-line stars in our sample mainly appear on the main-sequence, allowing a first estimate of the terminal-age main-sequence (TAMS) in the SMC, which matches the predicted TAMS between 12 and $40 M_{\odot}$ at SMC metallicity. We further find a large underabundance of stars above $\sim 25 M_{\odot}$ near the ZAMS, reminiscent of such earlier findings in the Milky Way and LMC.

Keywords: galaxies: Magellanic Clouds – galaxies: stellar content – stars: early-type – stars: emission-line, Be – stars: fundamental parameters

1. INTRODUCTION

The evolutionary path, lifetime and fashion in which massive stars ($> 8 M_{\odot}$; Poelarends et al. 2008) die are the foundation of many fields in astrophysics. The chemical composition and kinematics of galaxies are linked to massive star chemical yields, strong stellar winds, and supernova explosions (Ceverino & Klypin 2009; Kennicutt & Evans 2012). Astrophysical phenomena, such as long gamma ray bursts (Woosley & Bloom 2006) or gravitational waves (Marchant et al. 2016; Abbott et al. 2017), have been linked to the death of the most massive stars and black holes left behind. Moreover, the reionization of the Universe has also been suggested to be controlled by very low metallicity massive stars (Haiman & Loeb 1997). Nevertheless, the stellar evolution of massive O- and B-type stars is not well understood, a lack

of knowledge that worsens for the most massive stars ($> 100 M_{\odot}$; Vink et al. 2015), particularly at the stage of core helium burning (Langer 2012).

To make significant improvements in stellar evolution computations, unbiased empirical anchors and large surveys are essential. For many decades, photometric studies were the main source of information to explore large samples of massive stars (e.g. Fitzpatrick & Garmany 1990; Massey 2002); however, those studies were limited in generating useful constraints (Larsen et al. 2011). For instance, they could not define the shape of the main-sequence band in the Hertzsprung-Russell diagram (HRD), and did not show the presence of a clear transition between the main-sequence and the He-burning supergiant phases. Moreover, the position and number of B-type supergiants, apparently in post main-sequence, He-burning stages, challenge the theoretical predictions (Vink et al. 2010).

The new generation of multi-object spectrographs, large telescopes, and state-of-the-art stellar atmosphere codes have allowed successful, extended surveys focused

Corresponding author: Norberto Castro
 ncastro@umich.edu

on the analyses of massive stars in the Galaxy, such as the IACOB (Simón-Díaz et al. 2017), MIMES (Wade et al. 2014), and BOB (Morel et al. 2014) surveys; and in the Large Magellanic Cloud (LMC), the VFTS project (Evans et al. 2011). This wealth of spectroscopic data provides new insights on stellar evolution compared to previous photometric studies, thus providing the required empirical constraints (e.g. Martins & Palacios 2017; Ramírez-Agudelo et al. 2017; Sabín-Sanjulián et al. 2017; Simón-Díaz et al. 2017). In Castro et al. (2014), we showed how it is possible to highlight patterns in the spectroscopic Hertzsprung-Russell diagram (sHRD; $\mathcal{L} \equiv T_{\text{eff}}^4/g$, Langer & Kudritzki 2014) and proposed empirical anchors, such as the position of the zero age main-sequence (ZAMS) and of the terminal age main-sequence (TAMS), based on large collections of stellar atmosphere studies in the Milky Way. Those empirical anchors can validate or refute the theoretical evolution of massive stars predicted using different approaches for the different evolutionary stages, and evaluate the role of fundamental parameters such as rotation, overshooting or metallicity (Brott et al. 2011; Ekström et al. 2012).

Metallicity is a fundamental parameter for stellar evolution. For instance, theory predicts that the duration of the hydrogen-burning phase depends on metallicity (Langer 2012; Georgy et al. 2013; Sanyal et al. 2017). Thus, large, quantitative stellar atmosphere studies are also mandatory in metal-poor environments, to constrain the role of chemical composition in stellar evolution. The Small Magellanic Cloud (SMC), due to its proximity (63 kpc, Graczyk et al. 2014; Scowcroft et al. 2016) and low metal content ($Z/Z_{\odot} \sim 0.2$, e.g., Trundle et al. 2007), is the best laboratory for this endeavor, and also extending the work of Castro et al. (2014). The Runaways and Isolated O-Type Star Spectroscopic Survey of the Small Magellanic Cloud (RIOTS4; Lamb et al. 2016) covers a large sample of field massive stars and provides an excellent spectroscopic sample to dissect the evolution of massive stars at the SMC metallicity. Here, we analyze the spectra of a large fraction of stars published by Lamb et al. (2016) and new targets observed during multi-epoch follow-ups in the SMC Wing carried out within the same project. The sample explored in this work includes 329 OB stars, which we quantitatively characterize in a homogeneous way.

This paper is structured as follows. Section 2 gives an overview of the data. Section 3 summarizes the stellar quantitative analysis and presents the results and locus of the stars in the sHRD. In Section 4, we explore the behavior of the Oe/Be stars vs normal main-sequence stars. Section 5 brings new insight on the mass discrep-

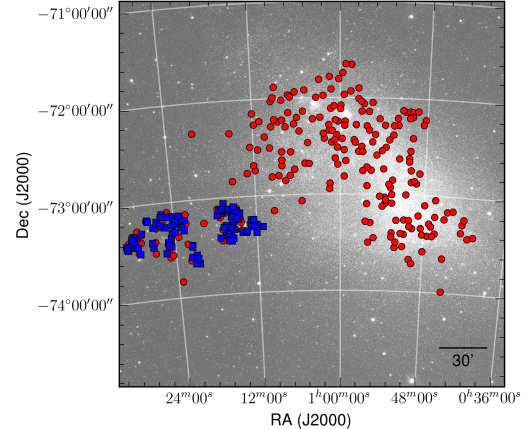


Figure 1. Distribution of the 329 OB stars targeted in this work across the SMC. The RIOTS4 stars published by Lamb et al. (2016) (223 stars) are marked with red dots. The additional new 106 stars from Evans et al. (2004) observed in the Wing are marked with blue squares. The gap between the targets in the Wing ($\text{RA} \sim 00^{\text{h}}20^{\text{m}}00^{\text{s}}$) results from optimizing the number of targets in the IMACS masks. The grayscale image is narrowband green continuum ($\lambda_c = 5130 \text{ \AA}$, $\Delta\lambda = 155 \text{ \AA}$) from the MCELS survey (Smith & MCELS Team 1998).

ancy problem for massive stars (Herrero et al. 1992). We discuss possible anchors to stellar evolution at low metallicity in Section 6. A final summary is presented in Section 7.

2. SMC FIELD OB STAR SAMPLE

We analyse 329 O and B-type stars in the SMC (Figure 1). The selected sample comprises of 223 stars previously classified by Lamb et al. (2016) and 106 stars newly observed in the SMC Wing, which were selected from the catalog of Evans et al. (2004) (see also Bonanos et al. 2010). The RIOTS4 survey consists of O- and early B-type stars selected according to the reddening-free index $Q_{\text{UBR}} \leq -0.84$ (Oey et al. 2004) and a magnitude cut of $B \leq 15.21$. Evans et al. (2004) observed primarily O-, B- and A-type stars in the SMC having $(B_J - R) < 0.1$, with a magnitude cut of $B_J \leq 17.51$. The fainter magnitude edge used by Evans et al. (2004) allows us to explore stars in a lower range of stellar masses ($< 20 M_{\odot}$) than the RIOTS4 sample (Section 6); most of the stars we targeted have $V < 16.5$.

Details about the instruments and spectroscopic data reduction for the previously classified 223 stars can be found in Lamb et al. (2016). The additional 106 OB stars in the SMC Wing were essentially observed in the same way, with the Inamori-Magellan Areal Camera and Spectrograph (IMACS, Bigelow & Dressler 2003) on the Magellan Baade telescope at Las Campanas Observa-

tory, Chile. The instrument was operated in multi-slit mode with the f/4 camera and 1200 lines/mm grating centered at approximately 4400 Å. This configuration provides a resolving power of $R \sim 3000$ and a wavelength coverage spanning from 3600 to 5200 Å, for a slit centered in the field; the actual wavelength coverage for each object depends on the position of the slit in the multi-object mask. Each field was observed with three exposures of 1200 seconds each. We obtain an average S/N ratio of 90, and ~ 50 for the faintest targets ($V = 17.7$). The S/N is generally high enough to perform quantitative analysis of the stellar atmospheres for the whole sample.

The new data in the SMC Wing were, in the first instance, reduced using the dedicated COSMOS pipeline¹ (Dressler et al. 2011; Oemler et al. 2017) for IMACS in multi-object spectroscopic mode. COSMOS spectra were then individually extracted and wavelength-calibrated in a second step using standard IRAF² tasks for long-slit spectroscopic data reduction.

3. STELLAR SPECTROSCOPIC ANALYSIS

We follow the same general approach described by Urabeja et al. (2005) for the analysis of B-type supergiants in NGC 300 and Castro et al. (2012) for those in NGC 55 (see also Evans et al. 2007), in which we search for the best set of stellar parameters that simultaneously reproduce the main observed lines. The spectroscopic quantitative analysis is based on a grid of stellar atmosphere models generated with the atmosphere/line formation code FASTWIND (Santolaya-Rey et al. 1997; Puls et al. 2005; Rivero González et al. 2012). The code takes into account non-local thermodynamic equilibrium in spherical symmetry, with an explicit treatment of the stellar wind, ensuring a smooth transition between the pseudo-static photosphere and the inner wind layers.

We built a new FASTWIND grid including only H I, He I and He II atomic models (Jokuthy 2002; Puls et al. 2005, see below). Effective temperatures are sampled from 9000 to 67000 K in steps of 1000 K and surface gravity ($\log g$) from 0.8 to 5.0 dex in steps of 0.1 dex. At large spectral luminosities ($\mathcal{L} \equiv T_{\text{eff}}^4/g$; Langer & Kudritzki 2014), i.e., close to the Eddington limit ($\log \mathcal{L}/\mathcal{L}_\odot = 4.6$), and T_{eff} lower than approximately 10000 K, the FASTWIND code has convergence problems

¹ <http://code.obs.carnegiescience.edu/cosmos>.

² IRAF is distributed by the National Optical Astronomy Observatory, which is operated by the Association of Universities for Research in Astronomy, Inc., under cooperative agreement with the National Science Foundation.

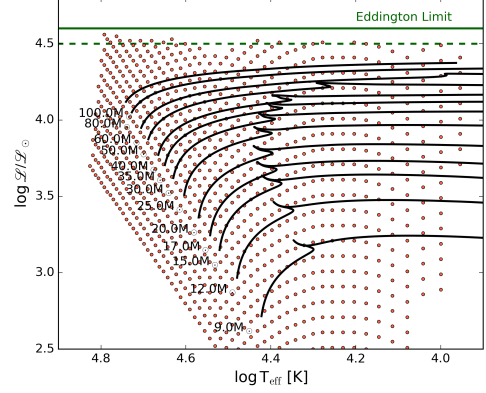


Figure 2. Coverage of the FASTWIND stellar grid built in this work (red dots) across the sHRD (Langer & Kudritzki 2014) together with stellar evolutionary tracks for rotating (150 km s⁻¹) stars by Brott et al. (2011) computed for the SMC metallicity (black solid lines). The Eddington limit ($\log \mathcal{L}/\mathcal{L}_\odot = 4.6$) and the convergence limit of the grid are marked with green solid and dashed lines, respectively.

and these models are discarded. Figure 2 shows the distribution of the grid in the sHRD.

Since previous studies did not report any strong age/metallicity gradient between the main body of the SMC and the Wing (e.g. Dobbie et al. 2014; Dias et al. 2016), we adopted the SMC average metallicity. Due to the low metallicity and average initial mass of our sample (Sect. 6), strong stellar winds are not expected (Kudritzki & Puls 2000; Mokiem et al. 2006; Nieva & Przybilla 2012) and a wind strength parameter $\log Q = -14$ was used (Puls et al. 1996; Kudritzki & Puls 2000). Three surface helium abundances (He/H, by number) were set as 0.1 (solar), 0.15 and 0.25. Three values of microturbulence (10, 15 and 20 km s⁻¹) were also considered. The modest spectral resolution of the data and the small sensitivity of the analysed He lines to He abundance variations does not allow us to constrain the abundance of He. Similarly, the lack of metal transitions in most of the analysed stars does not allow us to constrain microturbulence velocity. However, both quantities have been left free to vary to avoid computational biases that may result from forcing these parameters. They do not have any significant impact on the results.

Projected rotational velocities ($v \sin i$) are estimated by fitting the helium spectral features, adopting rotation and the instrument resolution as the only broadening mechanisms for the FASTWIND synthetic lines. Based on a first-guess synthetic model, we fit the radial velocities and $v \sin i$'s by convolving and cross-matching the synthetic lines until the observations are reproduced. Sub-

sequently, new synthetic models are calculated based on the newly estimated radial velocities and $v \sin i$'s. This process is iterated until convergence. We caution that we have not considered macroturbulence in the line profile broadening, but the line profile shapes and stellar parameters are robust at our low spectral resolution (80 km s^{-1}). The $v \sin i$ for our sample will be presented in another work currently under way (Paggeot et al., in preparation).

Due to the SMC's low metallicity and low spectral resolution, only a few of the observed stars show metallic transitions. For example, only $\sim 11\%$ of the complete sample shows Si III $\lambda 4552$ having equivalent width (EW) $> 0.15 \text{ \AA}$ (see Table 1), and it mostly appears in giants and supergiants. The lack of metallic lines for most of the stars therefore prevents the simultaneous use of metallic ionization states (e.g., Si IV/Si III) and fitting Balmer-line wings to constrain effective temperatures T_{eff} and surface gravities respectively (e.g. McErlean et al. 1999). Therefore, in order to analyze the sample with a single, uniform method, we explore only the H and He lines in this work. The strongest features in the spectra are the hydrogen Balmer lines, He I features at $\lambda\lambda 4016, 4121, 4144, 4388, 4471$ and 4713 and, in stars earlier than B0, He II features at $\lambda\lambda 4200, 4541$ and 4686 .

Figure 3 displays the synthetic EW of three principal diagnostic H and He lines in the analysis across our FASTWIND grid. Mid-, late O-type, and early B-type stars can be characterized by the ratio of He II and He I transitions (e.g., Holgado et al. 2017). Figure 4 complements Fig. 3 and shows the dependence of He II and H γ EW with the effective temperature for four spectroscopic luminosities. Figures 3 and 4 demonstrate that using exclusively the H and He ionization states and Balmer line profiles, while less than ideal, still yields quantitative leverage on simultaneous fitting of the T_{eff} and \mathcal{L} .

At the edges of the grid and where the Balmer lines provide poor leverage, mainly between B supergiants, we expect large degeneracies in the parameters; these are reflected in the errors extracted from our analysis.

We compare the observed hydrogen and helium lines with those in the grid. We use a similar χ^2 grid approach to the one described in Castro et al. (2012) (see also Lefever et al. 2010). The size of the grid and the speed of the analysis allow us to compare the data with the complete grid without requiring any optimization technique. The algorithm allows us to explore the probability distribution across the entire grid, thus identifying and discarding any secondary χ^2 minima. Note the analysis is based on the same element transitions

(H, He) and without considering any prior spectral classifications (Lamb et al. 2016; Evans et al. 2004), thus generating homogeneous analysis across the sample.

Figure 5 displays the outcome of the analysis for five hot stars, where the He II transitions provide the main temperature criteria. We see that the errors in the temperature and gravity are small when He II and He I transitions are both clearly visible in the data. On the other hand, for the hottest star in Figure 5, [M2002] SMC 38024, a wider range of parameters can reproduce the observed H I and He II lines, while He I is absent. Figure 6 shows the same as Figure 5, but for five B-type stars. Because of the weakness or absence of He II lines and Balmer line strengths (Figs 3 and 4), our algorithm and grid provide solid constraints for the gravities and T_{eff} that reproduce the observed data. In particular, although using only H and He, our analysis confirms that stars showing Si III $\lambda 4552$ are giant and supergiant B-type stars (Table 1), where the peak strength of this line is expected (Lennon et al. 1993), thus demonstrating why we are not able to detect this line below $\sim 25 M_{\odot}$. The stellar parameters derived for the 329 stars are listed in Table 1, along with the errors reflecting the limitations of the analysis being based on only H, He. Further consequences are discussed below (Sect. 4).

A large fraction of the sample shows emission in the Balmer lines (Sect. 4), owing to their Oe/Be nature (e.g., Golden-Marx et al. 2016; Lamb et al. 2016). We manually trim out the core of the Balmer lines when emission is detected by visual inspection of each spectrum. The cores of the lines are excluded from the spectroscopic analysis. H γ and H δ are less contaminated than H β , and also less affected by the trimming of their cores; this effectively gives them appropriately larger weights in the analysis. The Oe/Be stars are identified in the last column of Table 1.

The binary fraction in the sample is unknown, but it is expected to be high (Sana et al. 2012; Moe & Di Stefano 2017). Spectra with clear binary profiles are removed from the sample; however, we caution that the presence of undetected binaries may have unknown effects on our results. Our multi-epoch survey in the SMC Wing, which will allow us to constrain the binary population, is still ongoing and results will be published elsewhere.

Figure 7 shows the sHRD, which is constructed from the T_{eff} and $\log g$ values, and is independent of distance and extinction. Based on the SMC distance of 63 kpc (Graczyk et al. 2014; Scowcroft et al. 2016), we also estimate stellar luminosities (Table 1) on the basis of the derived synthetic FASTWIND spectral energy distributions and Massey (2002) optical photometry adopting

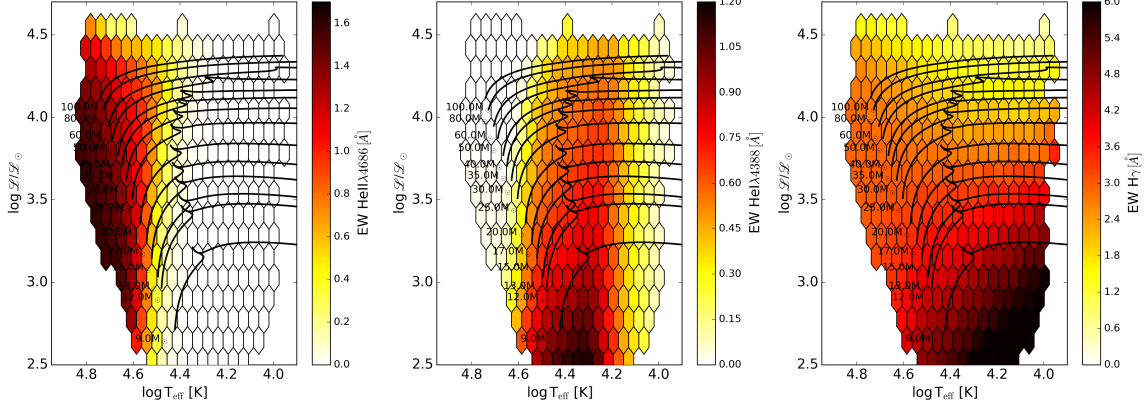


Figure 3. From left to right, synthetic He II $\lambda 4686$, He I $\lambda 4387$ and $H\gamma$ equivalent widths (EW) predicted by the FASTWIND stellar atmosphere code. Evolutionary tracks Brott et al. (2011) for rotating (150 km s^{-1}) are also displayed (black solid lines).

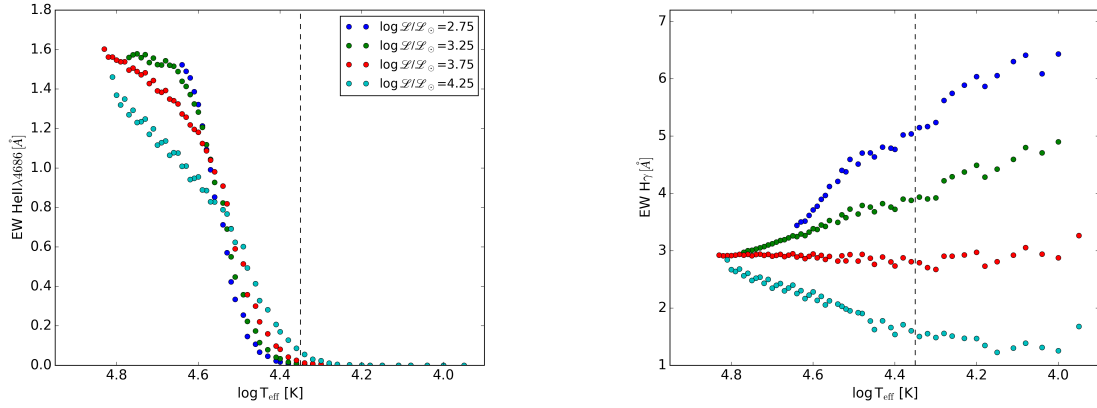


Figure 4. Dependence of He II $\lambda 4686$ and $H\gamma$ EW with the effective temperature for four spectroscopic luminosities across the distributions shown in Fig. 3. The approximated temperature where He I transitions reach the largest EW, i.e. $\log T_{\text{eff}} [\text{K}] \sim 4.35$, is marked (black dashed lines).

the SMC extinction (Gordon et al. 2003). We caution that due to the SMC’s depth to the line of sight (e.g., Ripepi et al. 2017), the uncertainty on photometric luminosities is up to 0.3 dex; on the other hand, $\mathcal{L}/\mathcal{L}_\odot$ is independent of distance. The photometric HRD is shown in the right panel of Figure 7.

4. ASSIGNMENT OF BE STARS IN THE SHRD

The SHRD shows a peculiar bimodal distribution for our 329 stars: we find 231 stars around $\log T_{\text{eff}} [\text{K}] \sim 4.45$ and a second group of 98 stars at $\log T_{\text{eff}} [\text{K}] \sim 4.15$. Both diagrams, the sHRD and HRD, qualitatively agree for stars at $\log T_{\text{eff}} [\text{K}] > 4.3$ and masses between 12 and $40 M_\odot$, placing most of these stars on the main sequence. However, there is a significant discrepancy for the objects at $\log T_{\text{eff}} [\text{K}] < 4.3$. While the sHRD places the stars between the 9 and $25 M_\odot$ tracks, in contrast, in the HRD, even though they are based on the same T_{eff} values, these stars fall below the $12 M_\odot$ track (see Sect. 5). The right panel of Figure 7 compares the photometric

luminosities obtained by Massey (2002) with our estimations. The stellar sample published by Massey (2002) shows two distinct, dense areas in the HRD: one below the theoretical ZAMS and another that matches the position of our main-sequence objects at approximately $20 M_\odot$.

We find that the population of stars at $\log T_{\text{eff}} [\text{K}] \leq 4.3$ largely corresponds to emission-line stars. There are 73 classical Be stars, as classified by Lamb et al. (2016) at these temperatures. Figure 8 highlights the close correspondence between the position of the stars in the sHRD and the presence/absence of emission in the Balmer lines. We find several objects non-classified as emission stars at $\log T_{\text{eff}} [\text{K}] \leq 4.3$. These may in fact be Be stars that have not yet been identified as such (see Sect. 5). Note that the Oe/Be classifications are determined spectroscopically and are independent of our stellar atmosphere spectroscopic analysis.

Figure 9 shows five Be stars in the sample where the core of the Balmer lines are partially filled by the cir-

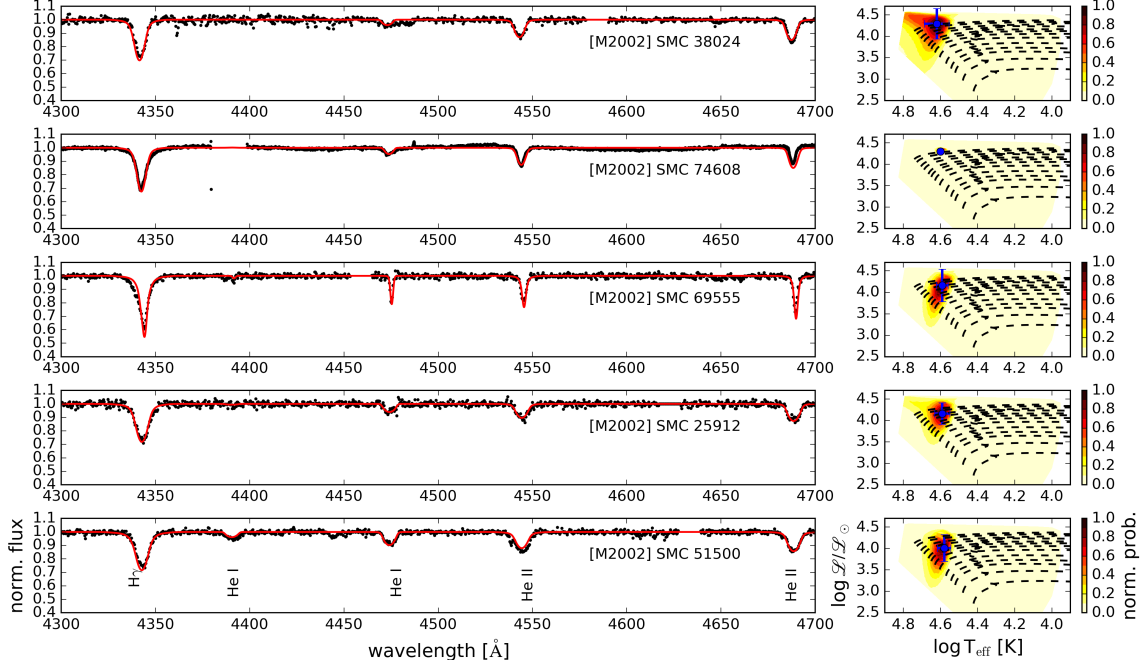


Figure 5. Outcome of the analysis for five O-type stars in our sample. Left: best fitting FASTWIND models (red) in our grid overlaid on the observed spectra (black). The main transitions in the plotted wavelength range are labeled at the bottom. Gaps in the data are due to separations between the detectors in the IMACS mosaic. Right: probability distributions in the sHRD extracted from the synthetic grid. The best solution is marked by a blue dot. Evolutionary tracks for rotating, single stars with SMC metallicity (Brott et al. 2011) are also shown (black dashed lines).

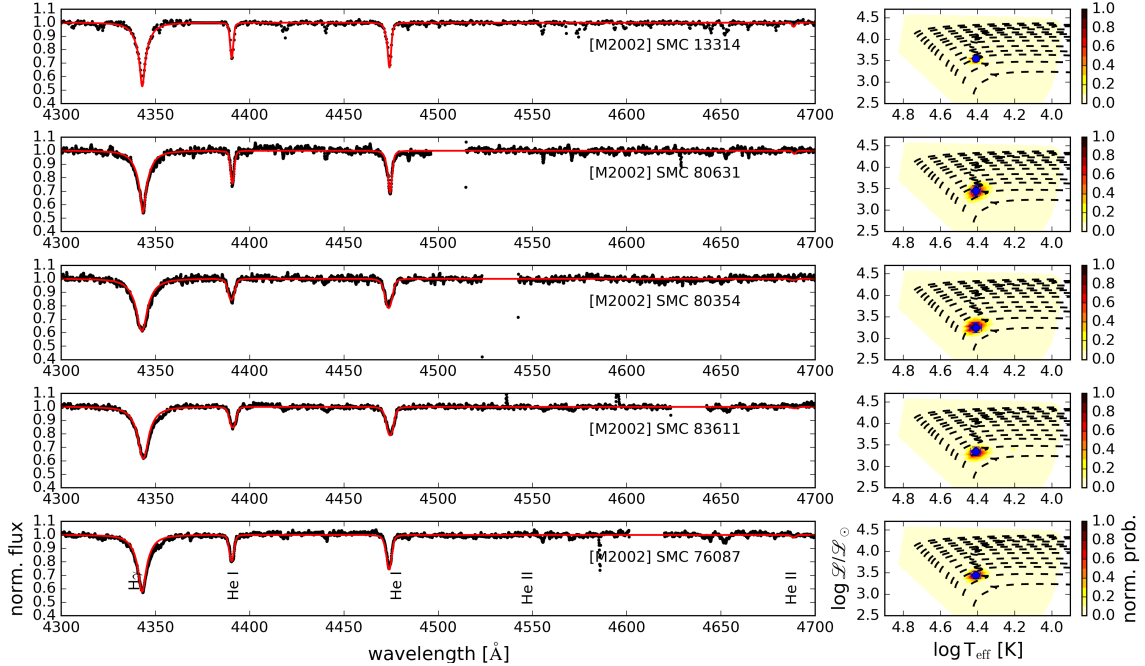


Figure 6. Outcome of the analysis for five B-type stars in the sample, shown as in Figure 5.

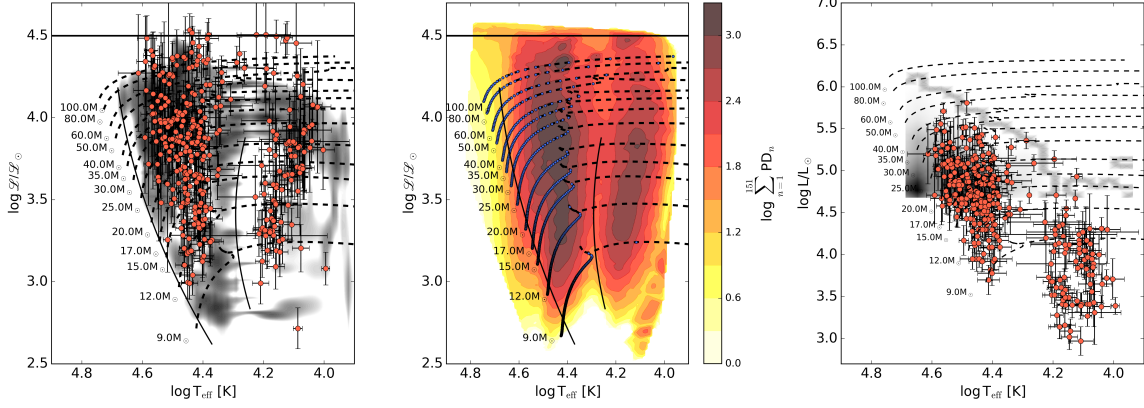


Figure 7. Left: position in the SHRD of the SMC stars analyzed in this work (red dots) overplotted on the empirical Milky Way SHRD (Castro et al. 2014) (grayscale). T_{eff} and \mathcal{L} have been slightly shifted (0.015 dex in both axes) up or down to decrease overlapping, and thus clearly show the density distribution. Middle: sum of all the probability distribution functions (see right panels in Fig. 5). The solid horizontal line at $\log \mathcal{L}/\mathcal{L}_{\odot} = 4.5$ marks the limit of the grid; note that the Eddington limit is at $\log \mathcal{L}/\mathcal{L}_{\odot} = 4.6$. The Milky Way empirical ZAMS and TAMS published by Castro et al. (2014) are marked by black solid lines. The blue dots indicate equal time steps separated by 0.1 Myr. Right: position of the sample stars in the HRD. Photometric luminosities from Massey (2002, see his Figure 10) are shown by the grayscale. In all panels, evolutionary tracks for rotating (150 km s $^{-1}$) single star with SMC metallicity (Brott et al. 2011) are shown by black dashed lines.

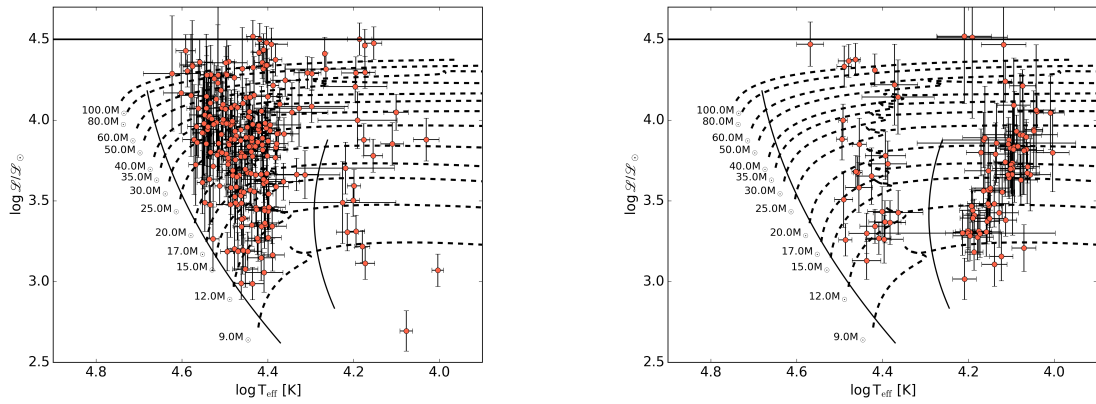


Figure 8. Our sample is split into non-emission stars in the left panel, and Oe/Be stars as classified by Lamb et al. (2016) in the right panel. The solid lines are as in Figure 7.

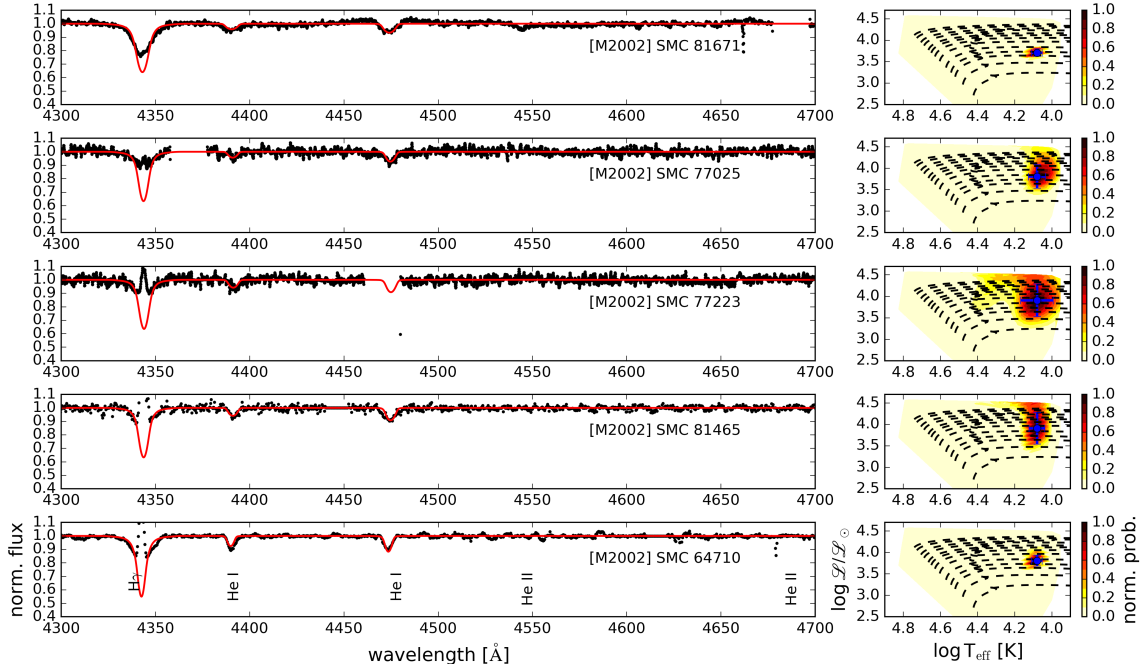


Figure 9. Outcome of the analysis for five emission stars in the sample, shown as in Figure 5.

cumstellar emissions, and trimmed out before the analysis. The absence of He II lines discards large temperatures for these five stars. Despite the degeneracy shown in Fig. 3, the He I lines and the remaining H Balmer absorption provide tighter probability distributions in temperature and gravity (Fig. 4) than expected from the lack of metallic transitions in the analysis.

Be stars are slightly evolved, but generally remain on the main sequence (Rivinius et al. 2013), so their location on the sHRD apparently beyond the Hertzsprung gap is suspicious. The RIOTS4 survey selection criteria were meant to obtain O- and early B-type stars (Section 2). The left panel of Figure 10 shows the full sample in the sHRD and the selection boundary predicted by FASTWIND synthetic spectral energy distributions corresponding to the RIOTS4 $Q_{UBR} < -0.84$ color criterion (solid grey line). The Q_{UBR} selection edge corresponds to the theoretical TAMS (Brott et al. 2011), and discards stars at $\log T_{\text{eff}}[\text{K}] < 4.3$ in the sample. Could the Be stars meet the selection criteria because of enhanced R -band flux from H α emission? The black solid line in Figure 10 shows that an excess of 0.5 mag in R is needed to shift the selection boundary to the shown locus, a value that is unphysically large. Thus, H α emission is not responsible for the appearance of Be stars in the cooler region of the sHRD. We also examined the effect of extinction in the synthetic photometry, as derived from the stellar positions in the sHRD. The right panel in Figure 10 shows that extinction also cannot re-

produce the observed Q_{UBR} values, and thus is also not responsible for the objects appearing at $\log T_{\text{eff}}[\text{K}] < 4.3$.

Therefore, the Be star positions on the sHRD are misplaced, and their actual positions should be at higher T_{eff} and lower \mathcal{L} . This is further confirmed by the fact that their published spectral types are in the range B0 – B1 (Lamb et al. 2016), the same as those of their correctly placed counterparts (Fig. 11). The reason for the misplacement is due partly to the H, He grid used in this work, and the application of the analysis technique to these emission-line stars. He I lines reach their maximum strength at $T_{\text{eff}} \sim 20000$ K (e.g. Lennon et al. 1993), and on either side of this temperature it is possible to find similar He I EW (Fig. 3). It is therefore difficult to distinguish the temperatures slightly above and below this value in the absence of other criteria, in particular, the standard metallic ions used for spectroscopic classification. In our analysis, the temperature degeneracy can be broken by the He II diagnostic and the Balmer EW. However, for the Be stars (Fig. 9), our spectroscopic analysis apparently improperly selects the cooler T_{eff} and higher \mathcal{L} . The cooler values cannot be correct, as they do not match the photometry and photometric selection criteria as demonstrated by Fig. 10. Moreover, the stars in the cool sequence are assigned high, supergiant \mathcal{L} that are inconsistent with their observed photometric luminosities (Fig. 7), but which would be consistent with main-sequence positions at the hotter T_{eff} . Yet, our attempt to force the analysis to recover the correct temperature by removing models cooler than

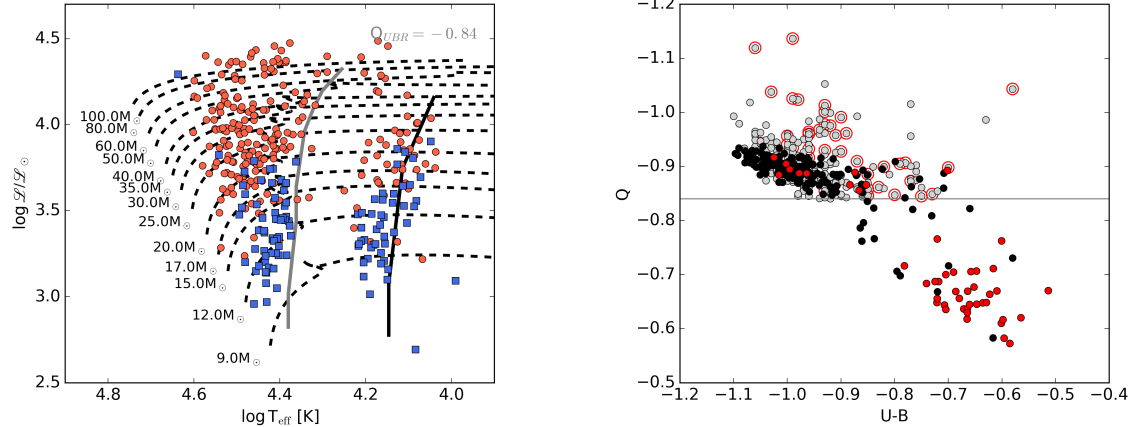


Figure 10. Left: sHRD for our stars showing RIOTS4 with red dots and those from Evans et al. (2004) with blue dots. The solid gray line shows the $Q_{UBR} < -0.84$ RIOTS4 selection criterion as derived from synthetic FASTWIND photometry; the black solid line shows the shift in the same selection criterion assuming an additional excess in the R -band of 0.5 magnitudes. Right: Observed photometry of RIOTS4 stars (gray dots), which are selected according to $Q_{UBR} < -0.84$ (solid line). Observed emission stars are encircled (red). The FASTWIND synthetic values for the same stars, calculated according to the stellar parameters listed in Table 1 (black dots), including reddening, are also shown, with black and red dots showing non-Oe/Be stars and Oe/Be stars, respectively.

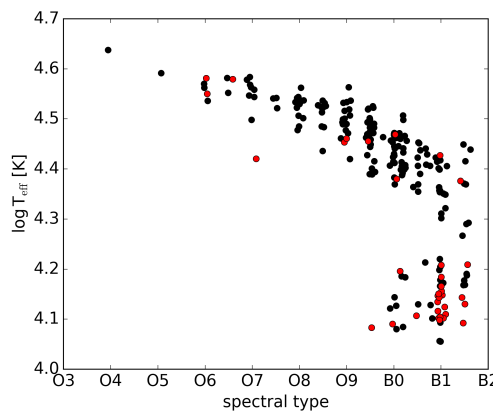


Figure 11. The $\log T_{\text{eff}} [\text{K}]$ obtained from spectroscopic analysis vs observed spectral type for the RIOTS4 sample classified by Lamb et al. (2016). The stars at $\log T_{\text{eff}} [\text{K}] < 4.3$ generate a bimodality in spectral type due to being misplaced in $\log T_{\text{eff}} [\text{K}]$. Black and red dots display non-Oe/Be and Oe/Be stars respectively.

$\log T_{\text{eff}} [\text{K}] = 4.35$ from the grid failed. The stars maintained incorrect, cool temperature values, suggesting an unaccounted for effect in these model atmospheres.

5. NEW INSIGHT ON THE MASS-DISCREPANCY PROBLEM

We extract stellar masses according to their respective positions in the sHRD and HRD, and interpolating between the available Brott et al. (2011) tracks. Those stars outside of the parameter space covered by the evolutionary tracks, in particular, stars above $100 M_\odot$ (Fig. 7) are discarded. Figure 12 quantifies the differ-

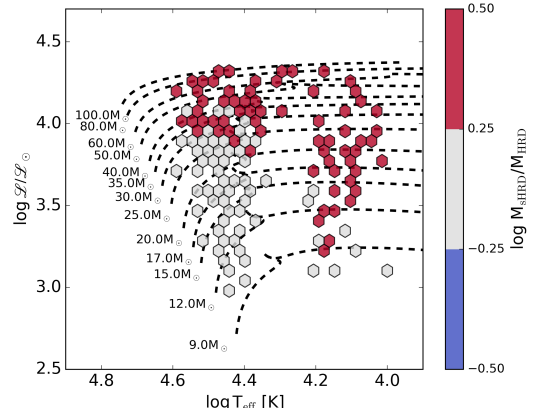


Figure 12. Discrepancy between the masses predicted by the positions of the stars in the sHRD and HRD. Each hexabin shows the median mass ratio of all stars within it. Note that stars in Figure 7 lying outside of the evolutionary tracks boundaries (i.e., $> 100 M_\odot$) are not included in this plot.

ence in masses derived from these two methods. We find large discrepancies for the Be stars at $\log T_{\text{eff}} [\text{K}] < 4.3$, and also for the most massive stars ($> 40 M_\odot$): the masses predicted by the sHRD are up to 50% larger than from the HRD.

The mass discrepancy in the upper part of the sHRD is a long-standing problem; spectroscopically-determined masses are well known to be systematically lower than those obtained from evolutionary tracks (e.g. Herrero et al. 1992; Weidner & Vink 2010; Markova & Puls 2015). Recently, Sabín-Sanjulián et al. (2017) reported O-type stars in the LMC with masses that are larger

when inferred from the Kiel diagram ($\log g$ vs $\log T_{\text{eff}}$) versus those derived from the HRD. The [Sabín-Sanjuán et al. \(2017\)](#) discrepancies increased at masses $> 30 M_{\odot}$ (see their figure 13), following the same trend found in our study. The problem is worst for the highest-mass stars, which have the strongest stellar winds and mass loss. [Herrero et al. \(1992\)](#) suggest that an increase in the overshooting parameter for the stellar evolution models can reduce the discrepancy (see also [Markova et al. 2018](#)).

However, the fact that we now see a similar effect for classical Be stars may point to a common origin for the problem. Both groups of stars have outer envelopes that tend to be gravitationally unbound: in the case of the highest-mass stars, due to the Eddington limit ([Sanyal et al. 2015](#); cf. Sect 6); and for Be stars, due to extreme rotation velocities ([Rivinius et al. 2013](#)). Therefore, it appears that the atmosphere models may be omitting an effect, perhaps related to extreme mass loss or envelope structure in this regime. For example, He II $\lambda 4686$ is sensitive to the presence of winds, which cause this line to go into emission. Since the presence of photospheric He II is a critical diagnostic for selecting hotter temperatures for Be stars, its absence by circumstellar emission wind infill can misplace the star to the cool, but luminous region of the sHRD. A preliminary experiment increasing the mass-loss rate by an order of magnitude does not change the qualitative results, and a comprehensive study is needed to determine whether mass-loss plays a role in resolving the problem.

Alternatively, the mass discrepancy problem for the high-luminosity stars may be unrelated to that for the Be stars, which could conceivably be caused if we have not adequately removed the circumstellar emission from the photospheric line profiles. However, we find no distinction in the locus of weak vs strong Be stars in the cool sHRD sequence, and in particular Be stars are misplaced into the cool sequence on the sHRD *even if there is no detected emission in the analyzed lines*,

We note that Fig. 8 shows the presence of a few stars in the misplaced Be regime of the sHRD that are not classified as Be stars. We suggest that these in fact may be weak Be stars that only have emission in H α , and therefore are not yet identified as emission-line stars. Similar studies conducted for Milky Way stars ([Castro et al. 2014](#)) also present a population of stars at $\log T_{\text{eff}}[\text{K}] \sim 4.15$ (see also [Simón-Díaz et al. 2017](#)). Could some of these Galactic stars also correspond to unidentified emission-line stars in these studies? In addition to the possibility of Balmer emission existing outside of the observed wavelength range, the emission is often cyclic and may temporarily vanish ([Rivinius et al.](#)

[2013](#)). The Milky Way's population at $\log T_{\text{eff}}[\text{K}] < 4.3$ could not be quantitatively compared to that of this work because of the lack of reliable distances and information about Balmer emission. Stellar distances from the *GAIA* mission will allow us to pursue a similar detailed analysis in the Milky Way. High spectral resolution stellar atmosphere analyses of classical Be stars in a similar mass range are fundamental to clearly understand the origin of the misleading parameters found in this work.

6. MAIN-SEQUENCE EMPIRICAL ANCHORS AT THE SMC METALLICITY

Almost all the stars we classified as non-emission stars are still burning hydrogen in the core according to their position on the sHRD and the stellar evolutionary tracks at SMC metallicity computed by [Brott et al. \(2011\)](#) (Figure 7). Here, we discuss three features in the distribution of these stars which may provide important constraints for the evolution of low metallicity massive stars.

First, we find an offset between the youngest stars ($\log T_{\text{eff}}[\text{K}] > 4.55$) and the theoretical ZAMS, which is most pronounced for stars above $\sim 30 M_{\odot}$. This lack of the hottest and most luminous O-type stars close to the ZAMS coincides with a similar dearth of stars in the Milky Way ([Castro et al. 2014](#)), and in the 30 Doradus region of the LMC ([Schneider et al. 2018](#)). It is striking since stellar evolution models predict the largest residence time of stars to be closest to the ZAMS. In principle, the simultaneous fitting of T_{eff} and surface gravity ([Schneider et al. 2017](#)) could result in an underestimate of $\log g$ and T_{eff} . However, [Holgado et al. \(2017\)](#) found a similar lack of stars close to the predicted ZAMS using high spectral resolution and S/N in a large sample of O-type stars in the Milky Way. Whereas high extinction of the youngest massive stars still being embedded in their birth clouds could be responsible, [Yorke \(1986\)](#) argues that the pre-main sequence contraction time scale becomes shorter than the accretion time scale for the highest mass stars. This would imply that the most massive stars would ignite hydrogen burning while still being in the accretion process, such that the concept of a ZAMS would not hold any more. As the dearth of hot O stars is observed in a large diversity of environments, its interpretation in terms of star formation history appears unlikely. Its occurrence at various metallicities argues that also envelope inflation ([Sanyal et al. 2015](#)) can not explain these observations. Also the shift of the ZAMS due to metallicity effects, which is less than 2000 K when comparing Solar and SMC metallicity models ([Brott et al. 2011](#)) is too insignificant.

Our second observed feature concerns the TAMS for stars in the mass range 10 to $40 M_{\odot}$. While in principle the sample selection criteria for the RIOTS4 sample (Sect. 4) could be responsible for the observed main-sequence low- T_{eff} limit (Fig. 10), this is mitigated by our inclusion of stars from Evans et al. (2004), which are selected according to different criteria. Evans et al. (2004)'s selected stars show the same empirical trend of the low- T_{eff} limit in the sHRD as the RIOTS4 sample in the mass range of overlap (Fig. 10). We therefore tentatively identify this low- T_{eff} limit as the TAMS.

The corresponding TAMS effective temperature of about $\log T_{\text{eff}}[\text{K}] = 4.3$ is almost 5000 K hotter than the Milky Way TAMS derived in a similar way by Castro et al. (2014). This matches the theoretical predictions by Brott et al. (2011), in particular between about 10 and $40 M_{\odot}$. Brott et al. (2011) calibrated the convective core overshooting parameter using tracks for rotating stars at masses around $16 M_{\odot}$. Above $15 M_{\odot}$ a slight enhancement of the overshooting parameter has been suggested to improve the match between observations and the theoretical tracks for the Milky Way, which would imply a mass-dependent overshooting parameter (Doom 1985; Castro et al. 2014). As noted above, this may also help with the mass discrepancy problem.

Finally, Fig. 7 shows an interesting feature for stars above roughly $30 M_{\odot}$. Whereas the distribution of the Galactic stars show a plume extending to very low temperatures above $\log \mathcal{L}/\mathcal{L}_{\odot} = 4.0$, the SMC stellar distribution shows a void to the redward of $\log T_{\text{eff}} = 4.3$ up to much higher values of $\mathcal{L}/\mathcal{L}_{\odot}$ (see Fig. 8). Interpreting the cool luminous stars in terms of envelope inflation (Sanyal et al. 2015) would allow the conclusion that this phenomenon occurs only at much higher masses in the SMC, compared to the Milky Way, as predicted by (Sanyal et al. 2017). Unfortunately, the gravities of the most luminous stars in the sHRD are not reliable, as discussed in Sect. 5. Therefore, additional studies are required before this feature can be used as a solid empirical constraint for evolutionary models at this high mass range.

7. SUMMARY

We present a comprehensive stellar atmosphere analysis of 329 O- and B-type stars in the SMC selected from the RIOTS4 (Lamb et al. 2016) and Evans et al. (2004) surveys. Due to the lack of metal lines at SMC metallicity, our quantitative analysis is rooted on a hydrogen and helium FASTWIND model atmosphere grid. On the resulting sHRD, the majority of stars (231) lie at $\log T_{\text{eff}}[\text{K}] > 4.3$, but the rest of the sample (98 stars) is located at $\log T_{\text{eff}}[\text{K}] \sim 4.15$. We find that the latter

population is mainly composed of classical Be stars. The spectroscopic analysis misplaces these stars to unrealistically low temperatures and gravities, incorrectly placing them beyond the theoretical main-sequence. Calculating luminosities and masses, this misplacement causes substantial mass discrepancies for these Be stars at low T_{eff} , and also high-luminosity stars. We quantify the discrepancy by extracting evolutionary masses according to the position of the stars and evolutionary tracks of Brott et al. (2011) for rotating stars. Strong mass discrepancies are found for the most massive stars ($> 40 M_{\odot}$), confirming the well-known mass-discrepancy problem (e.g., Markova et al. 2018), but now also for the emission-line stars seen in the sHRD at $\log T_{\text{eff}}[\text{K}] < 4.3$. Since both groups showing this discrepancy are near the limit of gravitational binding, we suggest that the atmosphere models omit an effect related to mass loss or envelope structure in this regime, thereby underestimating the gravities and T_{eff} extracted from our grid. Spectroscopic observations at UV wavelengths would be desirable to constrain stellar winds in the sample (e.g., Garcia et al. 2014).

The HRD and sHRD show a good qualitative match for stars at $\log T_{\text{eff}}[\text{K}] > 4.3$ and masses lower than approximately $40 M_{\odot}$. The shape of the stellar distribution at $\log T_{\text{eff}}[\text{K}] > 4.3$ on the sHRD qualitatively matches that predicted by Brott et al. (2011)'s evolutionary tracks at SMC metallicity. As in previous studies in the Milky Way (e.g., Holgado et al. 2017), we find a dearth of stars close to the ZAMS at higher masses. Either there are no very young stars in these samples, or they are highly extincted at optical wavelengths. At the end of the main sequence, the sample traces well the theoretical TAMS predicted by Brott et al. (2011)'s tracks at the SMC metallicity, between 12 and $40 M_{\odot}$. Above $\sim 15 M_{\odot}$, a slight enhancement of the core overshooting parameter would improve the agreement between observations and theory, suggesting a mass-dependent overshooting parameter. Above $40 M_{\odot}$, stars may match the extended main sequence to low temperatures as predicted by Brott et al. (2011). However, due to the significant mass discrepancy problem in this regime, and thus the uncertainty of T_{eff} and $\log g$, we can not firmly establish a TAMS location at this high mass. In any case, the apparent absence of $25 - 40 M_{\odot}$ stars to the right of the predicted TAMS (Fig. 8) indicates that envelope inflation due to the proximity to the Eddington limit may be weaker in the SMC, compared to the Milky Way, in line with the expectation (Sanyal et al. 2017).

Large spectroscopic datasets are key to exploring the stellar evolution of massive stars at different evolutionary stages and environments. The study presented here

is complementary to the work of Castro et al. (2014) and adds new insight on stellar evolution at SMC metallicity. Further spectroscopic studies are needed to clarify

how stellar winds and circumstellar material are altering our analyses, and to obtain information on other factors affecting evolution, such as binarity.

Table 1. OB sample in the SMC analyzed in this work.

M2002 ID	RA (J2000)	Dec (J2000)	$\log T_{\text{eff}}$	$\log \mathcal{L}$	$\log L$	$\log M_{\text{sHRD}}$	$\log M_{\text{HRD}}$	Oe/Be	Metals
	[h, m, s]	[$^{\circ}$, ' $'$, ''']	[K]	[\mathcal{L}_{\odot}]	[L_{\odot}]	[M_{\odot}]	[M_{\odot}]		
38024	00 56 44.17	-72 03 31.3	4.62 ± 0.07	4.29 ± 0.36	5.2 ± 0.19	—	1.49	—	-
74608	01 13 42.41	-73 17 29.3	4.6 ± 0.01	4.3 ± 0.05	5.71 ± 0.19	—	1.66	—	-
69555	01 09 25.46	-73 09 29.7	4.59 ± 0.03	4.16 ± 0.38	5.07 ± 0.19	1.79	1.41	—	-
51500	01 01 32.79	-72 16 45.3	4.58 ± 0.04	4.01 ± 0.31	4.67 ± 0.24	1.61	1.32	—	-
25912	00 53 09.34	-72 53 30.6	4.59 ± 0.04	4.16 ± 0.25	5.18 ± 0.25	1.79	1.45	—	-
9732	00 48 00.63	-73 34 37.9	4.58 ± 0.03	3.91 ± 0.35	5.08 ± 0.3	1.52	1.4	—	-
21877	00 51 58.86	-72 16 38.3	4.58 ± 0.02	3.71 ± 0.25	5.02 ± 0.3	1.41	1.38	—	-
47478	00 59 54.05	-72 04 31.2	4.57 ± 0.03	3.87 ± 0.34	4.71 ± 0.18	1.51	1.3	—	-
43724	00 58 33.20	-71 55 46.8	4.57 ± 0.03	4.07 ± 0.3	5.23 ± 0.21	1.68	1.44	—	-
40380	00 57 27.96	-72 00 26.1	4.56 ± 0.03	4.32 ± 0.27	5.26 ± 0.31	—	1.45	—	-
83510	01 30 16.63	-73 20 51.6	4.56 ± 0.02	4.02 ± 0.19	4.58 ± 0.25	1.62	1.27	—	-
15690	00 50 10.02	-73 15 39.0	4.56 ± 0.02	4.32 ± 0.17	5.47 ± 0.3	—	1.52	—	-
7437	00 46 42.17	-73 24 55.2	4.56 ± 0.02	4.42 ± 0.05	5.56 ± 0.19	—	1.56	—	-
67060	01 07 59.87	-72 00 53.9	4.56 ± 0.02	4.02 ± 0.26	4.93 ± 0.19	1.62	1.34	—	-
60460	01 04 53.21	-72 40 33.7	4.54 ± 0.02	3.87 ± 0.27	4.76 ± 0.18	1.46	1.28	—	-
68756	01 08 56.01	-71 52 46.5	4.54 ± 0.02	4.07 ± 0.25	5.04 ± 0.21	1.66	1.36	—	-
24982	00 52 53.45	-72 55 31.9	4.53 ± 0.02	3.92 ± 0.28	4.83 ± 0.21	1.48	1.29	—	-
46035	00 59 20.69	-72 17 10.3	4.54 ± 0.02	4.27 ± 0.18	5.04 ± 0.21	1.9	1.36	—	-
35598	00 56 01.66	-72 08 24.6	4.54 ± 0.02	3.97 ± 0.32	4.61 ± 0.25	1.57	1.26	—	-
77368	01 16 57.55	-73 19 26.6	4.57 ± 0.03	4.37 ± 0.14	5.31 ± 0.18	—	1.48	—	-
35491	00 55 59.62	-72 19 54.0	4.54 ± 0.02	3.97 ± 0.3	5.08 ± 0.22	1.57	1.38	—	-
7782	00 46 56.18	-73 18 57.0	4.53 ± 0.02	4.12 ± 0.25	5.08 ± 0.31	1.68	1.37	—	-
15271	00 50 01.77	-72 11 26.0	4.57 ± 0.03	4.47 ± 0.14	5.49 ± 0.19	—	1.54	e	-
75210	01 14 22.52	-73 13 23.2	4.54 ± 0.02	3.87 ± 0.22	5.08 ± 0.19	1.46	1.38	—	-
36514	00 56 17.32	-72 17 28.4	4.54 ± 0.01	3.47 ± 0.18	4.88 ± 0.21	1.29	1.31	—	-
17240	00 50 39.92	-72 59 43.3	4.54 ± 0.04	4.07 ± 0.46	5.13 ± 0.21	1.66	1.4	—	-
13896	00 49 33.21	-73 42 18.3	4.53 ± 0.02	4.12 ± 0.19	5.34 ± 0.18	1.68	1.46	—	-
36325	00 56 14.25	-72 42 56.0	4.53 ± 0.01	3.62 ± 0.2	5.27 ± 0.31	1.34	1.43	—	-
40341	00 57 26.99	-72 33 13.3	4.52 ± 0.03	4.27 ± 0.63	5.15 ± 0.18	1.89	1.38	—	-
72941	01 12 05.82	-72 40 56.2	4.53 ± 0.02	3.72 ± 0.22	4.7 ± 0.19	1.38	1.25	—	-
48170	01 00 10.62	-71 48 05.9	4.53 ± 0.02	3.62 ± 0.37	5.12 ± 0.22	1.34	1.39	—	-
81586	01 24 42.75	-73 09 04.2	4.53 ± 0.01	3.82 ± 0.13	4.7 ± 0.25	1.43	1.25	—	-
21844	00 51 58.37	-73 15 48.7	4.53 ± 0.02	4.22 ± 0.36	5.27 ± 0.31	1.84	1.43	—	-

Table 1 continued

Table 1 (*continued*)

M2002 ID	RA (J2000)	Dec (J2000)	$\log T_{\text{eff}}$	$\log \mathcal{L}$	$\log L$	$\log M_{\text{sHRD}}$	$\log M_{\text{HRD}}$	Oe/Be	Metals
	[h, m, s]	[$^{\circ}, ^{\prime}, ^{\prime\prime}$]	[K]	[\mathcal{L}_{\odot}]	[L_{\odot}]	[M_{\odot}]	[M_{\odot}]		
64773	01 06 51.15	-72 33 21.7	4.52 ± 0.02	3.97 ± 0.17	4.65 ± 0.21	1.56	1.23	–	–
6946	00 46 23.88	-73 12 52.1	4.52 ± 0.01	3.27 ± 0.2	5.07 ± 0.31	1.19	1.35	–	–
34005	00 55 33.93	-72 02 43.3	4.52 ± 0.02	3.77 ± 0.27	4.65 ± 0.24	1.38	1.23	–	–
1600	00 42 10.00	-73 13 56.2	4.51 ± 0.01	4.11 ± 0.14	4.88 ± 0.25	1.69	1.28	–	–
46317	00 59 27.42	-72 48 36.7	4.52 ± 0.02	3.97 ± 0.21	4.83 ± 0.21	1.56	1.27	–	–
46831	00 59 38.58	-71 44 18.7	4.52 ± 0.02	3.97 ± 0.18	4.83 ± 0.31	1.56	1.27	–	–
81646	01 24 51.16	-73 27 01.6	4.52 ± 0.01	4.07 ± 0.19	4.98 ± 0.25	1.65	1.32	–	–
65346	01 07 06.96	-72 08 46.5	4.52 ± 0.01	4.27 ± 0.1	4.65 ± 0.24	1.89	1.23	–	–
70149	01 09 48.19	-72 30 19.0	4.52 ± 0.01	3.57 ± 0.17	4.94 ± 0.21	1.3	1.31	–	–
67269	01 08 06.09	-72 33 00.9	4.52 ± 0.01	3.97 ± 0.15	4.94 ± 0.31	1.56	1.31	–	–
69598	01 09 26.78	-72 01 26.4	4.51 ± 0.02	4.01 ± 0.25	4.66 ± 0.31	1.6	1.22	–	–
48672	01 00 22.18	-72 30 48.5	4.52 ± 0.01	4.17 ± 0.11	4.89 ± 0.19	1.75	1.29	–	–
51435	01 01 31.20	-72 20 07.6	4.52 ± 0.01	3.87 ± 0.15	4.72 ± 0.21	1.44	1.25	–	–
50791	01 01 14.74	-71 54 30.8	4.52 ± 0.02	4.27 ± 0.18	4.65 ± 0.25	1.89	1.23	–	–
77253	01 16 48.02	-73 09 26.2	4.52 ± 0.01	3.47 ± 0.12	4.58 ± 0.19	1.25	1.21	–	–
50825	01 01 15.68	-72 06 35.4	4.51 ± 0.02	4.11 ± 0.21	4.53 ± 0.26	1.69	1.19	–	–
11045	00 48 30.80	-72 15 59.0	4.51 ± 0.01	4.01 ± 0.1	4.53 ± 0.24	1.6	1.19	–	–
43411	00 58 27.13	-71 39 00.9	4.49 ± 0.01	3.86 ± 0.17	4.87 ± 0.31	1.45	1.27	–	–
28153	00 53 49.41	-72 16 44.0	4.49 ± 0.02	3.76 ± 0.17	4.83 ± 0.24	1.39	1.26	–	–
39211	00 57 06.09	-72 01 59.1	4.51 ± 0.01	3.81 ± 0.16	4.72 ± 0.24	1.39	1.24	–	–
62416	01 05 39.78	-72 20 27.0	4.49 ± 0.02	3.86 ± 0.19	4.96 ± 0.32	1.45	1.31	–	–
49580	01 00 43.94	-72 26 04.9	4.49 ± 0.01	3.86 ± 0.13	5.04 ± 0.22	1.45	1.33	e	–
68071	01 08 31.85	-72 14 23.7	4.51 ± 0.01	3.61 ± 0.12	4.45 ± 0.24	1.3	1.17	–	–
75126	01 14 17.13	-73 15 49.2	4.51 ± 0.01	4.01 ± 0.1	5.51 ± 0.32	1.6	1.53	e	–
76657	01 16 00.03	-73 25 54.1	4.49 ± 0.02	3.96 ± 0.21	4.61 ± 0.18	1.52	1.19	–	–
75626	01 14 50.86	-73 06 48.8	4.51 ± 0.01	3.81 ± 0.15	4.66 ± 0.24	1.39	1.22	–	–
76553	01 15 52.11	-73 20 48.6	4.49 ± 0.03	3.76 ± 0.0	5.52 ± 0.25	1.39	1.53	–	–
75929	01 15 11.44	-72 50 15.5	4.49 ± 0.02	4.36 ± 0.13	5.81 ± 0.23	–	1.67	e	–
80998	01 23 21.08	-73 49 51.7	4.49 ± 0.05	4.36 ± 0.01	4.83 ± 0.25	–	1.26	–	–
46022	00 59 20.46	-72 14 25.3	4.49 ± 0.02	3.86 ± 0.24	4.87 ± 0.31	1.45	1.27	–	–
72884	01 12 02.55	-72 08 49.3	4.49 ± 0.01	3.96 ± 0.09	4.67 ± 0.18	1.52	1.21	–	–
76371	01 15 39.23	-73 23 49.1	4.49 ± 0.01	3.96 ± 0.17	5.11 ± 0.19	1.52	1.35	–	–
22451	00 52 08.06	-73 32 47.6	4.49 ± 0.02	3.96 ± 0.18	5.11 ± 0.31	1.52	1.35	–	–
79248	01 19 39.78	-73 14 49.4	4.49 ± 0.01	4.26 ± 0.07	4.87 ± 0.24	1.88	1.27	–	–
49825	01 00 50.01	-72 04 58.7	4.49 ± 0.01	3.86 ± 0.14	4.78 ± 0.31	1.45	1.25	–	–
15742	00 50 11.13	-72 32 34.8	4.48 ± 0.02	4.3 ± 0.22	5.27 ± 0.21	1.92	1.42	–	–
83678	01 30 50.23	-73 22 59.4	4.49 ± 0.01	4.36 ± 0.06	5.4 ± 0.24	–	1.48	–	–
53373	01 02 19.01	-72 22 04.4	4.49 ± 0.01	4.26 ± 0.11	5.08 ± 0.19	1.88	1.34	–	–
81941	01 25 35.72	-73 11 11.1	4.49 ± 0.01	3.96 ± 0.13	5.08 ± 0.24	1.52	1.34	–	–

Table 1 continued

Table 1 (*continued*)

M2002 ID	RA (J2000)	Dec (J2000)	$\log T_{\text{eff}}$	$\log \mathcal{L}$	$\log L$	$\log M_{\text{sHRD}}$	$\log M_{\text{HRD}}$	Oe/Be	Metals
	[h, m, s]	[$^{\circ}, '$, "]	[K]	[\mathcal{L}_{\odot}]	[L_{\odot}]	[M_{\odot}]	[M_{\odot}]		
83017	01 28 47.62	-73 18 23.1	4.48 ± 0.01	3.9 ± 0.2	4.61 ± 0.25	1.47	1.19	-	-
42260	00 58 05.62	-72 26 04.0	4.49 ± 0.01	3.76 ± 0.15	4.92 ± 0.25	1.39	1.28	-	-
71871	01 11 08.08	-73 19 09.7	4.48 ± 0.02	3.5 ± 0.18	4.17 ± 0.32	1.21	1.09	-	-
53042	01 02 10.88	-72 25 05.3	4.46 ± 0.01	3.94 ± 0.13	4.71 ± 0.22	1.47	1.2	-	-
82511	01 27 09.74	-73 27 12.9	4.48 ± 0.02	3.2 ± 0.12	0.0 ± 0.0	1.13	-	-	-
83767	01 31 06.91	-73 24 45.9	4.48 ± 0.01	3.6 ± 0.14	4.72 ± 0.3	1.25	1.21	-	-
17813	00 50 49.93	-73 24 21.9	4.48 ± 0.02	3.2 ± 0.14	4.55 ± 0.32	1.13	1.18	-	-
14878	00 49 54.38	-72 24 37.2	4.48 ± 0.01	4.1 ± 0.09	5.02 ± 0.24	1.62	1.32	-	-
71815	01 11 05.62	-72 13 41.7	4.48 ± 0.02	4.0 ± 0.11	4.42 ± 0.25	1.52	1.14	-	-
81647	01 24 51.22	-73 06 00.4	4.48 ± 0.01	3.8 ± 0.16	4.67 ± 0.25	1.43	1.2	-	-
71002	01 10 26.06	-72 23 28.9	4.48 ± 0.01	4.0 ± 0.09	5.09 ± 0.21	1.52	1.34	-	-
24096	00 52 37.85	-72 22 52.6	4.48 ± 0.02	3.7 ± 0.26	5.15 ± 0.31	1.33	1.36	-	m
76253	01 15 31.64	-73 14 59.7	4.48 ± 0.02	3.5 ± 0.22	4.55 ± 0.19	1.21	1.18	-	-
82322	01 26 35.28	-73 15 16.4	4.48 ± 0.01	3.9 ± 0.12	4.86 ± 0.24	1.47	1.26	-	-
6908	00 46 22.64	-73 23 17.1	4.48 ± 0.02	3.7 ± 0.2	5.37 ± 0.32	1.33	1.45	-	-
53319	01 02 17.71	-71 58 33.7	4.48 ± 0.01	3.9 ± 0.09	4.61 ± 0.24	1.47	1.19	-	-
16230	00 50 20.57	-72 37 02.6	4.48 ± 0.01	4.1 ± 0.11	5.4 ± 0.32	1.62	1.46	-	-
45677	00 59 13.41	-72 39 02.2	4.46 ± 0.02	4.34 ± 0.25	5.18 ± 0.19	-	1.37	-	-
81169	01 23 47.91	-73 13 35.0	4.45 ± 0.03	3.78 ± 0.22	4.49 ± 0.25	1.36	1.13	-	-
61039	01 05 05.76	-72 08 06.9	4.46 ± 0.02	4.04 ± 0.12	4.28 ± 0.23	1.6	1.09	-	-
19382	00 51 17.41	-73 23 48.6	4.46 ± 0.02	3.84 ± 0.12	5.13 ± 0.31	1.4	1.35	-	-
76640	01 15 58.60	-73 22 46.2	4.46 ± 0.02	3.64 ± 0.15	4.36 ± 0.19	1.26	1.12	-	m
76796	01 16 10.66	-73 08 00.5	4.46 ± 0.02	3.54 ± 0.14	4.11 ± 0.21	1.22	-	-	-
62981	01 05 57.49	-72 11 54.5	4.46 ± 0.02	3.34 ± 0.12	4.76 ± 0.24	1.15	1.22	-	-
63877	01 06 23.15	-72 15 53.5	4.46 ± 0.01	3.54 ± 0.14	4.71 ± 0.3	1.22	1.2	-	-
81019	01 23 25.15	-73 22 00.9	4.45 ± 0.04	4.18 ± 0.24	4.74 ± 0.25	1.7	1.2	-	-
11802	00 48 48.54	-73 12 30.2	4.46 ± 0.01	3.84 ± 0.15	4.96 ± 0.22	1.4	1.28	-	-
72724	01 11 53.32	-72 44 14.6	4.46 ± 0.02	3.64 ± 0.12	4.85 ± 0.21	1.26	1.25	-	-
77816	01 17 37.36	-73 06 41.7	4.45 ± 0.01	3.88 ± 0.1	4.78 ± 0.19	1.44	1.22	-	-
73337	01 12 28.97	-72 29 29.2	4.46 ± 0.01	4.14 ± 0.12	5.43 ± 0.19	1.77	1.47	-	-
13075	00 49 15.88	-72 52 43.4	4.46 ± 0.01	4.04 ± 0.13	5.51 ± 0.21	1.6	1.51	-	-
38893	00 57 00.19	-72 30 09.8	4.46 ± 0.02	3.84 ± 0.16	4.76 ± 0.22	1.4	1.22	e	-
16481	00 50 25.57	-72 08 02.8	4.46 ± 0.01	4.04 ± 0.14	4.8 ± 0.19	1.6	1.23	-	-
67334	01 08 08.00	-72 38 19.8	4.45 ± 0.06	3.78 ± 0.25	4.7 ± 0.31	1.36	1.19	-	-
48601	01 00 20.37	-72 41 22.3	4.45 ± 0.01	4.08 ± 0.07	5.15 ± 0.25	1.58	1.35	-	-
15102	00 49 58.78	-73 39 48.0	4.45 ± 0.04	3.58 ± 0.15	5.03 ± 0.31	1.23	1.3	-	m
82783	01 27 57.71	-73 10 15.0	4.45 ± 0.02	3.98 ± 0.12	4.49 ± 0.25	1.49	1.13	-	-
54456	01 02 45.57	-72 12 05.9	4.45 ± 0.03	3.88 ± 0.14	5.18 ± 0.21	1.44	1.37	-	-
24213	00 52 39.74	-73 05 12.1	4.45 ± 0.01	3.78 ± 0.08	4.86 ± 0.21	1.36	1.24	-	-

Table 1 continued

Table 1 (*continued*)

M2002 ID	RA (J2000)	Dec (J2000)	$\log T_{\text{eff}}$	$\log \mathcal{L}$	$\log L$	$\log M_{\text{sHRD}}$	$\log M_{\text{HRD}}$	Oe/Be	Metals
	[h, m, s]	[$^{\circ}, ^{\prime}, ^{\prime\prime}$]	[K]	[\mathcal{L}_{\odot}]	[L_{\odot}]	[M_{\odot}]	[M_{\odot}]		
29312	00 54 10.40	-72 32 30.0	4.45 ± 0.02	3.58 ± 0.09	4.37 ± 0.25	1.23	1.1	-	-
27496	00 53 37.41	-72 30 35.4	4.45 ± 0.01	3.68 ± 0.1	4.6 ± 0.21	1.27	1.17	-	-
1037	00 41 33.13	-73 25 32.2	4.45 ± 0.01	3.38 ± 0.07	4.6 ± 0.24	1.15	1.17	-	-
51384	01 01 29.85	-72 56 26.2	4.41 ± 0.03	4.15 ± 0.16	5.12 ± 0.21	1.64	1.32	-	m
67029	01 07 58.92	-72 13 17.7	4.45 ± 0.02	3.48 ± 0.08	4.43 ± 0.24	1.2	1.12	-	-
68963	01 09 04.03	-72 12 58.2	4.45 ± 0.02	3.68 ± 0.2	4.43 ± 0.24	1.27	1.12	-	-
55952	01 03 18.95	-71 59 31.5	4.45 ± 0.01	3.68 ± 0.04	4.65 ± 0.24	1.27	1.18	e	-
13831	00 49 32.05	-72 51 16.4	4.45 ± 0.01	3.68 ± 0.08	5.0 ± 0.19	1.27	1.29	-	-
21983	00 52 00.62	-73 29 25.4	4.45 ± 0.02	4.38 ± 0.1	4.65 ± 0.25	-	1.18	e	-
83504	01 30 16.02	-73 21 26.7	4.45 ± 0.02	3.48 ± 0.17	0.0 ± 0.0	1.2	-	e	-
81870	01 25 24.55	-73 15 17.8	4.45 ± 0.02	3.48 ± 0.13	0.0 ± 0.0	1.2	-	-	-
81960	01 25 38.77	-73 07 07.9	4.45 ± 0.03	3.18 ± 0.12	4.3 ± 0.31	1.07	1.08	-	-
76066	01 15 20.14	-73 15 14.7	4.45 ± 0.04	3.28 ± 0.12	3.95 ± 0.21	1.11	1.03	e	-
76332	01 15 36.59	-73 11 57.7	4.45 ± 0.02	3.18 ± 0.09	4.3 ± 0.22	1.07	1.08	-	-
77178	01 16 40.79	-73 03 35.9	4.45 ± 0.03	2.98 ± 0.08	3.95 ± 0.19	1.04	1.03	-	-
76446	01 15 44.05	-73 27 04.0	4.45 ± 0.02	2.98 ± 0.09	4.22 ± 0.18	1.04	1.08	-	-
82548	01 27 17.74	-73 24 18.9	4.45 ± 0.03	3.58 ± 0.15	0.0 ± 0.0	1.23	-	e	-
76147	01 15 25.10	-73 07 41.9	4.45 ± 0.02	3.28 ± 0.09	4.14 ± 0.21	1.11	1.05	e	-
81551	01 24 37.73	-73 26 25.3	4.45 ± 0.02	3.18 ± 0.11	4.49 ± 0.32	1.07	1.13	-	-
74932	01 14 04.20	-73 22 03.1	4.45 ± 0.03	3.08 ± 0.11	4.14 ± 0.29	1.05	1.05	-	-
81491	01 24 31.12	-73 22 36.2	4.45 ± 0.03	3.18 ± 0.15	3.95 ± 0.22	1.07	1.03	-	-
83492	01 30 13.29	-73 25 46.1	4.45 ± 0.02	3.78 ± 0.09	4.7 ± 0.24	1.36	1.19	-	-
83484	01 30 11.73	-73 24 11.2	4.45 ± 0.02	3.68 ± 0.08	4.37 ± 0.25	1.27	1.1	-	-
83155	01 29 10.80	-73 30 17.9	4.45 ± 0.01	3.38 ± 0.12	4.3 ± 0.29	1.15	1.08	-	-
82444	01 26 56.92	-73 30 54.3	4.45 ± 0.02	3.78 ± 0.08	4.49 ± 0.25	1.36	1.13	-	-
66415	01 07 40.35	-72 50 59.6	4.45 ± 0.01	4.08 ± 0.08	5.34 ± 0.19	1.58	1.43	-	-
65318	01 07 06.27	-71 57 46.4	4.45 ± 0.01	4.38 ± 0.04	4.6 ± 0.24	-	1.17	e	-
4424	00 44 34.57	-73 09 34.9	4.45 ± 0.03	3.48 ± 0.2	4.74 ± 0.19	1.2	1.2	-	-
8609	00 47 25.82	-73 24 51.0	4.45 ± 0.01	3.88 ± 0.08	5.06 ± 0.31	1.44	1.31	-	m
17963	00 50 52.69	-73 15 24.7	4.45 ± 0.03	3.98 ± 0.2	4.6 ± 0.21	1.49	1.17	-	-
81999	01 25 44.42	-73 14 33.0	4.43 ± 0.04	3.32 ± 0.11	4.08 ± 0.33	1.1	1.03	e	-
41345	00 57 47.47	-72 16 40.5	4.43 ± 0.03	3.62 ± 0.14	4.3 ± 0.24	1.21	1.08	-	m
16147	00 50 19.10	-72 39 17.7	4.43 ± 0.01	4.12 ± 0.07	4.84 ± 0.25	1.69	1.21	-	-
3459	00 43 49.95	-73 09 02.4	4.43 ± 0.02	4.42 ± 0.06	5.21 ± 0.21	-	1.36	-	-
81696	01 24 57.82	-73 29 47.9	4.43 ± 0.05	3.82 ± 0.19	4.63 ± 0.24	1.33	1.17	-	-
54721	01 02 51.91	-71 48 24.7	4.43 ± 0.02	4.52 ± 0.08	5.4 ± 0.19	-	1.45	-	-
5041	00 45 01.92	-73 14 02.4	4.43 ± 0.0	4.32 ± 0.0	4.72 ± 0.31	1.94	1.19	-	-
18301	00 50 58.81	-72 08 16.3	4.43 ± 0.01	3.92 ± 0.08	4.63 ± 0.19	1.42	1.17	-	-
16518	00 50 26.05	-72 12 10.1	4.43 ± 0.0	4.32 ± 0.08	4.94 ± 0.18	1.94	1.23	e	-

Table 1 continued

Table 1 (*continued*)

M2002 ID	RA (J2000)	Dec (J2000)	$\log T_{\text{eff}}$	$\log \mathcal{L}$	$\log L$	$\log M_{\text{sHRD}}$	$\log M_{\text{HRD}}$	Oe/Be	Metals
	[h, m, s]	[$^{\circ}, ^{\prime}, ^{\prime\prime}$]	[K]	[\mathcal{L}_{\odot}]	[L_{\odot}]	[M_{\odot}]	[M_{\odot}]		
9467	00 47 53.40	-73 06 02.5	4.43 ± 0.01	4.32 ± 0.01	4.87 ± 0.31	1.94	1.21	-	-
69155	01 09 10.99	-71 59 16.2	4.41 ± 0.03	4.05 ± 0.15	4.66 ± 0.31	1.54	1.16	-	m
75394	01 14 34.97	-73 13 48.3	4.41 ± 0.03	3.15 ± 0.12	4.36 ± 0.19	1.04	1.08	e	-
81819	01 25 17.05	-73 15 24.8	4.41 ± 0.04	3.35 ± 0.14	0.0 ± 0.0	1.1	-	e	-
76002	01 15 15.54	-73 07 22.0	4.41 ± 0.01	3.55 ± 0.09	4.61 ± 0.19	1.2	1.14	-	-
74503	01 13 35.92	-73 22 12.9	4.41 ± 0.04	3.35 ± 0.13	0.0 ± 0.0	1.1	-	e	-
73625	01 12 43.69	-73 18 45.3	4.41 ± 0.02	3.65 ± 0.08	4.42 ± 0.22	1.23	1.09	-	-
72824	01 11 59.24	-73 17 38.7	4.41 ± 0.03	3.35 ± 0.13	3.82 ± 0.32	1.1	-	-	-
81209	01 23 53.77	-73 19 02.7	4.41 ± 0.03	3.15 ± 0.14	4.3 ± 0.31	1.04	-	-	-
81163	01 23 47.03	-73 10 55.7	4.41 ± 0.03	3.15 ± 0.09	4.47 ± 0.3	1.04	1.11	-	-
15060	00 49 57.84	-72 51 54.4	4.41 ± 0.01	3.85 ± 0.08	4.7 ± 0.25	1.37	1.17	-	m
10421	00 48 16.85	-72 12 58.3	4.41 ± 0.01	3.75 ± 0.1	4.57 ± 0.31	1.34	1.13	-	-
32449	00 55 07.83	-72 22 40.9	4.41 ± 0.05	3.95 ± 0.12	4.94 ± 0.31	1.44	1.25	-	m
28496	00 53 55.67	-72 43 58.8	4.41 ± 0.01	4.35 ± 0.0	0.0 ± 0.0	-	-	-	-
59421	01 04 30.11	-72 27 45.9	4.4 ± 0.03	3.98 ± 0.06	5.01 ± 0.19	1.45	1.28	-	m
82459	01 27 00.02	-73 14 41.0	4.41 ± 0.02	3.45 ± 0.1	4.17 ± 0.33	1.14	1.04	-	-
47029	00 59 43.55	-72 25 14.9	4.41 ± 0.03	3.85 ± 0.13	4.47 ± 0.25	1.37	1.11	-	-
60439	01 04 52.97	-71 54 49.2	4.41 ± 0.01	4.35 ± 0.0	4.91 ± 0.25	-	1.24	-	-
34457	00 55 42.37	-73 17 30.2	4.4 ± 0.01	4.48 ± 0.0	4.9 ± 0.19	-	1.23	-	-
27712	00 53 41.74	-73 01 30.8	4.41 ± 0.02	3.65 ± 0.1	4.57 ± 0.24	1.23	1.13	-	-
49450	01 00 40.88	-72 13 42.9	4.4 ± 0.03	3.88 ± 0.1	4.74 ± 0.21	1.37	1.18	-	m
30018	00 54 24.64	-73 01 00.7	4.41 ± 0.01	4.35 ± 0.0	4.61 ± 0.3	-	1.14	-	-
69630	01 09 28.29	-72 17 14.7	4.41 ± 0.02	3.85 ± 0.09	4.84 ± 0.31	1.37	1.21	-	-
80545	01 22 11.24	-73 26 51.9	4.41 ± 0.03	3.95 ± 0.14	5.1 ± 0.25	1.44	1.32	-	m
10671	00 48 22.48	-73 20 19.5	4.41 ± 0.02	3.85 ± 0.08	4.81 ± 0.31	1.37	1.2	-	-
10129	00 48 09.78	-73 24 13.0	4.41 ± 0.06	3.85 ± 0.24	4.94 ± 0.24	1.37	1.25	-	-
27600	00 53 39.51	-73 05 37.9	4.41 ± 0.01	3.95 ± 0.06	5.02 ± 0.25	1.44	1.28	-	m
68157	01 08 34.63	-72 47 47.3	4.41 ± 0.01	3.85 ± 0.1	4.36 ± 0.19	1.37	1.08	-	-
25974	00 53 10.41	-72 25 48.2	4.15 ± 0.04	3.78 ± 0.19	4.02 ± 0.31	1.26	0.9	e	-
81673	01 24 55.21	-73 25 44.8	4.41 ± 0.04	3.45 ± 0.24	4.09 ± 0.31	1.14	1.02	-	-
82749	01 27 51.41	-73 09 53.5	4.41 ± 0.04	3.25 ± 0.15	0.0 ± 0.0	1.07	-	e	-
8257	00 47 14.39	-73 17 20.2	4.41 ± 0.02	3.65 ± 0.12	4.52 ± 0.25	1.23	1.12	-	-
80976	01 23 17.09	-73 09 35.6	4.41 ± 0.04	3.45 ± 0.14	0.0 ± 0.0	1.14	-	-	-
75254	01 14 25.43	-73 09 57.3	4.41 ± 0.04	3.05 ± 0.12	3.92 ± 0.33	1.02	0.98	-	-
80115	01 21 08.02	-73 38 48.8	4.41 ± 0.02	3.25 ± 0.09	4.24 ± 0.31	1.07	1.05	-	-
13314	00 49 20.70	-72 07 44.3	4.41 ± 0.01	3.55 ± 0.07	4.84 ± 0.32	1.2	1.21	-	m
80631	01 22 25.80	-73 11 57.4	4.41 ± 0.03	3.45 ± 0.12	4.3 ± 0.3	1.14	-	-	-
80354	01 21 40.83	-73 35 17.2	4.41 ± 0.03	3.25 ± 0.12	0.0 ± 0.0	1.07	-	-	-
83611	01 30 37.24	-73 25 14.9	4.41 ± 0.03	3.35 ± 0.1	4.52 ± 0.31	1.1	1.12	-	-

Table 1 continued

Table 1 (*continued*)

M2002 ID	RA (J2000)	Dec (J2000)	$\log T_{\text{eff}}$	$\log \mathcal{L}$	$\log L$	$\log M_{\text{sHRD}}$	$\log M_{\text{HRD}}$	Oe/Be	Metals
	[h, m, s]	[$^{\circ}, ^{\prime}, ^{\prime\prime}$]	[K]	[\mathcal{L}_{\odot}]	[L_{\odot}]	[M_{\odot}]	[M_{\odot}]		
76087	01 15 21.34	-73 08 54.4	4.41 ± 0.02	3.45 ± 0.09	4.36 ± 0.19	1.14	1.08	—	—
83699	01 30 54.74	-73 27 07.4	4.41 ± 0.03	3.45 ± 0.15	0.0 ± 0.0	1.14	—	e	—
77075	01 16 32.05	-73 23 13.9	4.41 ± 0.04	3.75 ± 0.14	3.92 ± 0.33	1.34	0.98	e	—
76245	01 15 31.07	-73 11 49.7	4.41 ± 0.03	3.25 ± 0.09	4.09 ± 0.19	1.07	1.02	e	—
83378	01 29 51.11	-73 24 59.4	4.41 ± 0.02	3.65 ± 0.16	0.0 ± 0.0	1.23	—	—	—
81380	01 24 17.30	-73 19 16.9	4.41 ± 0.03	3.35 ± 0.11	4.57 ± 0.3	1.1	1.13	—	—
83254	01 29 28.20	-73 26 05.9	4.41 ± 0.03	3.45 ± 0.13	4.24 ± 0.32	1.14	1.05	—	—
33823	00 55 30.57	-72 27 15.7	4.4 ± 0.04	4.48 ± 0.0	4.74 ± 0.3	—	1.18	—	—
83073	01 28 56.61	-73 23 12.3	4.41 ± 0.02	3.45 ± 0.13	4.42 ± 0.25	1.14	1.09	—	—
15263	00 50 01.66	-72 08 23.9	4.41 ± 0.03	3.95 ± 0.07	4.36 ± 0.25	1.44	1.08	—	—
76709	01 16 03.50	-73 08 36.8	4.41 ± 0.03	3.35 ± 0.1	4.01 ± 0.2	1.1	1.0	—	—
66160	01 07 32.52	-72 17 38.7	4.41 ± 0.01	3.95 ± 0.11	5.02 ± 0.21	1.44	1.28	—	m
81009	01 23 23.45	-73 14 15.1	4.41 ± 0.03	3.25 ± 0.13	4.17 ± 0.31	1.07	1.04	—	—
76482	01 15 46.64	-73 21 44.7	4.41 ± 0.02	3.45 ± 0.07	4.91 ± 0.19	1.14	1.24	—	—
76752	01 16 06.46	-73 22 05.3	4.41 ± 0.03	3.75 ± 0.14	4.7 ± 0.19	1.34	1.17	—	m
83229	01 29 23.86	-73 19 45.9	4.41 ± 0.04	3.65 ± 0.17	3.7 ± 0.24	1.23	0.95	e	—
80890	01 23 03.68	-73 11 38.0	4.41 ± 0.03	3.55 ± 0.12	4.09 ± 0.31	1.2	1.02	—	—
75233	01 14 23.91	-73 10 27.6	4.41 ± 0.02	3.35 ± 0.09	4.42 ± 0.21	1.1	1.09	—	—
48432	01 00 16.69	-72 14 34.2	4.41 ± 0.01	4.45 ± 0.01	4.3 ± 0.19	—	—	—	—
4919	00 44 57.05	-73 59 12.9	4.4 ± 0.01	4.38 ± 0.01	4.59 ± 0.19	—	1.14	—	—
1830	00 42 24.08	-73 16 51.2	4.4 ± 0.02	3.88 ± 0.06	5.03 ± 0.31	1.37	1.29	—	—
51234	01 01 25.98	-72 53 06.3	4.4 ± 0.07	3.98 ± 0.0	5.15 ± 0.25	1.45	1.34	—	m
73913	01 13 00.32	-73 17 03.7	4.41 ± 0.02	4.35 ± 0.07	5.17 ± 0.19	—	1.35	—	—
81519	01 24 34.37	-73 27 31.8	4.34 ± 0.05	3.66 ± 0.09	4.48 ± 0.31	1.2	1.08	—	—
63413	01 06 09.84	-71 56 00.7	4.43 ± 0.03	4.52 ± 0.01	5.3 ± 0.19	—	1.4	—	—
46392	00 59 29.08	-71 58 00.7	4.4 ± 0.03	3.78 ± 0.09	4.7 ± 0.31	1.31	1.18	—	—
34315	00 55 39.79	-72 45 01.7	4.38 ± 0.04	3.91 ± 0.14	4.98 ± 0.21	1.42	1.25	—	m
41648	00 57 53.87	-72 27 43.3	4.38 ± 0.01	4.11 ± 0.07	4.91 ± 0.19	1.56	1.22	—	m
77609	01 17 18.01	-73 12 00.3	4.38 ± 0.01	4.21 ± 0.09	5.4 ± 0.3	1.74	1.43	—	m
67305	01 08 07.21	-72 41 36.2	4.38 ± 0.05	4.21 ± 0.25	4.56 ± 0.21	1.74	1.1	e	—
80810	01 22 50.82	-73 16 07.2	4.38 ± 0.04	3.61 ± 0.11	4.22 ± 0.31	1.18	1.02	—	m
73169	01 12 19.45	-73 18 45.2	4.38 ± 0.05	3.81 ± 0.15	3.78 ± 0.31	1.38	0.92	e	—
75552	01 14 45.77	-73 13 38.4	4.38 ± 0.06	3.41 ± 0.14	3.95 ± 0.22	1.1	0.95	e	—
24056	00 52 37.15	-73 23 38.3	4.36 ± 0.08	4.14 ± 0.23	5.06 ± 0.21	1.62	1.29	e	m
63842	01 06 22.03	-72 44 09.4	4.36 ± 0.04	3.94 ± 0.06	4.56 ± 0.19	1.46	1.11	—	m
38302	00 56 49.32	-72 45 18.3	4.36 ± 0.08	4.04 ± 0.18	4.44 ± 0.19	1.52	1.07	—	—
19728	00 51 23.13	-72 07 20.6	4.32 ± 0.02	4.28 ± 0.07	5.28 ± 0.28	1.82	1.37	—	m
14190	00 49 39.63	-73 20 33.2	4.34 ± 0.08	3.66 ± 0.15	4.88 ± 0.31	1.2	1.21	—	—
31574	00 54 53.59	-72 35 29.6	4.34 ± 0.11	4.06 ± 0.24	4.48 ± 0.25	1.52	1.08	—	—

Table 1 continued

Table 1 (*continued*)

M2002 ID	RA (J2000)	Dec (J2000)	$\log T_{\text{eff}}$	$\log \mathcal{L}$	$\log L$	$\log M_{\text{sHRD}}$	$\log M_{\text{HRD}}$	Oe/Be	Metals
	[h, m, s]	[$^{\circ}, ^{\prime}, ^{\prime\prime}$]	[K]	[\mathcal{L}_{\odot}]	[L_{\odot}]	[M_{\odot}]	[M_{\odot}]		
28841	00 54 01.86	-73 07 09.3	4.36 ± 0.03	4.24 ± 0.08	4.86 ± 0.3	1.77	1.21	—	m
46241	00 59 25.57	-72 32 17.3	4.18 ± 0.09	4.0 ± 0.18	4.14 ± 0.31	1.56	0.94	—	—
15256	00 50 01.53	-72 44 36.0	4.41 ± 0.05	3.65 ± 0.14	4.87 ± 0.31	1.23	1.22	—	—
73952	01 13 01.91	-72 45 48.6	4.3 ± 0.03	4.3 ± 0.04	5.36 ± 0.19	1.86	1.41	—	m
20939	00 51 43.36	-72 37 24.9	4.3 ± 0.08	4.1 ± 0.07	4.54 ± 0.25	1.55	1.08	—	m
35474	00 55 59.25	-73 29 40.5	4.28 ± 0.0	4.41 ± 0.02	4.71 ± 0.3	—	1.15	—	m
50609	01 01 09.42	-72 27 28.4	4.26 ± 0.1	4.31 ± 0.05	5.09 ± 0.19	1.86	1.3	—	m
69769	01 09 33.51	-72 48 27.3	4.2 ± 0.11	3.71 ± 0.16	3.89 ± 0.22	1.22	0.86	—	—
38508	00 56 52.75	-72 33 19.8	4.23 ± 0.12	3.51 ± 0.25	4.39 ± 0.21	1.12	1.03	—	—
77814	01 17 37.14	-73 10 38.7	4.2 ± 0.03	3.31 ± 0.11	3.68 ± 0.19	1.01	0.81	e	—
65145	01 07 01.72	-72 47 54.8	4.15 ± 0.04	3.58 ± 0.14	3.54 ± 0.24	1.15	0.76	e	—
72868	01 12 01.88	-73 22 35.5	4.2 ± 0.02	3.11 ± 0.09	3.52 ± 0.18	0.9	0.76	—	—
80045	01 20 57.96	-73 34 14.5	4.2 ± 0.03	3.31 ± 0.12	3.68 ± 0.3	1.01	0.81	—	—
76179	01 15 27.37	-73 25 32.0	4.2 ± 0.02	3.61 ± 0.07	4.3 ± 0.21	1.16	1.0	—	—
76943	01 16 21.14	-73 08 32.8	4.18 ± 0.03	3.3 ± 0.14	3.14 ± 0.33	1.0	—	e	—
81682	01 24 56.05	-73 26 55.3	4.18 ± 0.04	3.3 ± 0.15	3.52 ± 0.26	1.0	0.76	e	—
24229	00 52 40.12	-72 59 44.3	4.18 ± 0.2	3.3 ± 0.17	4.24 ± 0.21	1.0	—	e	—
81840	01 25 20.52	-73 31 38.6	4.2 ± 0.02	3.31 ± 0.1	3.73 ± 0.31	1.01	0.82	—	—
83759	01 31 05.23	-73 26 35.1	4.2 ± 0.03	3.01 ± 0.13	0.0 ± 0.0	0.86	—	e	—
81720	01 25 01.22	-73 24 52.5	4.2 ± 0.04	3.31 ± 0.14	3.73 ± 0.31	1.01	0.82	e	—
72208	01 11 25.92	-72 31 20.9	4.2 ± 0.07	4.21 ± 0.05	5.14 ± 0.21	1.66	1.31	—	m
5063	00 45 03.31	-73 38 31.7	4.18 ± 0.03	3.8 ± 0.15	4.34 ± 0.21	1.28	1.01	e	—
40504	00 57 30.37	-71 53 47.4	4.15 ± 0.02	4.28 ± 0.08	4.22 ± 0.19	1.77	—	—	—
58947	01 04 19.88	-72 40 49.0	4.18 ± 0.01	3.9 ± 0.09	4.55 ± 0.21	1.39	1.08	—	m
76864	01 16 15.29	-73 07 05.2	4.18 ± 0.02	3.2 ± 0.11	3.28 ± 0.21	0.96	0.7	e	—
36175	00 56 11.50	-72 54 37.0	4.15 ± 0.02	4.48 ± 0.1	4.93 ± 0.19	—	1.22	—	m
80103	01 21 06.65	-73 39 31.1	4.18 ± 0.02	3.2 ± 0.09	0.0 ± 0.0	0.96	—	—	—
81145	01 23 43.80	-73 12 16.4	4.18 ± 0.03	3.5 ± 0.09	3.46 ± 0.2	1.12	0.75	e	—
79888	01 20 36.76	-73 39 47.0	4.18 ± 0.04	3.3 ± 0.14	3.14 ± 0.22	1.0	—	e	—
76683	01 16 01.75	-73 26 49.4	4.18 ± 0.02	3.3 ± 0.1	3.41 ± 0.25	1.0	0.73	e	—
81412	01 24 22.21	-73 08 41.5	4.15 ± 0.03	3.38 ± 0.14	3.09 ± 0.34	1.04	—	e	—
83232	01 29 24.03	-73 29 41.9	4.38 ± 0.03	3.91 ± 0.09	4.7 ± 0.25	1.42	1.15	—	—
82702	01 27 43.87	-73 10 45.5	4.18 ± 0.04	3.3 ± 0.14	0.0 ± 0.0	1.0	—	e	—
82279	01 26 28.22	-73 11 26.1	4.18 ± 0.02	3.4 ± 0.08	3.7 ± 0.31	1.06	0.81	e	—
77672	01 17 24.52	-73 07 21.8	4.18 ± 0.03	3.4 ± 0.11	3.61 ± 0.19	1.06	0.78	e	—
80127	01 21 09.38	-73 37 34.1	4.18 ± 0.01	3.5 ± 0.1	4.04 ± 0.3	1.12	0.91	—	—
82408	01 26 50.15	-73 23 45.8	4.15 ± 0.02	3.78 ± 0.1	4.02 ± 0.24	1.26	0.9	—	—
81243	01 23 59.46	-73 09 48.6	4.15 ± 0.05	3.48 ± 0.13	0.0 ± 0.0	1.1	—	e	—
11777	00 48 47.97	-72 46 24.5	4.18 ± 0.1	3.9 ± 0.17	4.36 ± 0.3	1.39	1.02	e	—

Table 1 continued

Table 1 (*continued*)

M2002 ID	RA (J2000)	Dec (J2000)	$\log T_{\text{eff}}$	$\log \mathcal{L}$	$\log L$	$\log M_{\text{sHRD}}$	$\log M_{\text{HRD}}$	Oe/Be	Metals
	[h, m, s]	[$^{\circ}, ^{\prime}, ^{\prime\prime}$]	[K]	[\mathcal{L}_{\odot}]	[L_{\odot}]	[M_{\odot}]	[M_{\odot}]		
77458	01 17 05.09	-73 26 36.0	4.18 ± 0.03	4.3 ± 0.07	4.71 ± 0.18	1.86	1.14	—	—
74367	01 13 26.34	-73 21 33.7	4.18 ± 0.03	3.4 ± 0.12	3.61 ± 0.19	1.06	0.78	e	—
22178	00 52 03.74	-72 12 16.8	4.18 ± 0.03	4.5 ± -0.0	4.47 ± 0.19	—	1.06	—	m
77397	01 16 59.72	-73 07 42.6	4.15 ± 0.03	3.28 ± 0.15	3.4 ± 0.21	0.98	0.72	e	—
80269	01 21 29.41	-73 27 55.7	4.15 ± 0.03	3.58 ± 0.08	3.4 ± 0.3	1.15	0.72	e	—
75061	01 14 13.19	-73 20 45.1	4.11 ± 0.02	3.95 ± 0.1	4.13 ± 0.19	1.41	0.93	e	m
75638	01 14 51.24	-73 08 14.2	4.15 ± 0.03	3.08 ± 0.14	3.49 ± 0.31	0.88	0.74	e	—
72656	01 11 49.86	-72 15 48.5	4.11 ± 0.03	3.35 ± 0.1	3.87 ± 0.31	1.02	0.85	e	—
76274	01 15 32.67	-73 19 05.8	4.15 ± 0.03	3.28 ± 0.15	3.49 ± 0.19	0.98	0.74	e	—
83412	01 29 58.16	-73 22 16.9	4.15 ± 0.03	3.38 ± 0.14	0.0 ± 0.0	1.04	—	e	—
15440	00 50 04.94	-73 19 31.1	4.11 ± 0.19	3.85 ± 0.25	4.27 ± 0.32	1.32	0.99	e	—
48882	01 00 27.03	-72 22 58.5	4.15 ± 0.04	3.58 ± 0.23	4.07 ± 0.25	1.15	0.92	e	—
24119	00 52 38.20	-73 26 16.8	4.15 ± 0.06	3.68 ± 0.21	4.12 ± 0.31	1.2	0.93	e	—
76604	01 15 55.31	-73 20 24.6	4.15 ± 0.03	3.48 ± 0.1	3.58 ± 0.18	1.1	0.77	e	—
36213	00 56 12.27	-73 05 50.8	4.15 ± 0.0	4.48 ± 0.01	4.67 ± 0.31	—	1.13	—	—
47551	00 59 55.63	-72 06 44.9	4.11 ± 0.02	4.25 ± 0.13	4.17 ± 0.25	1.72	0.95	e	—
83403	01 29 57.39	-73 19 28.2	4.15 ± 0.03	3.58 ± 0.15	0.0 ± 0.0	1.15	—	e	—
23954	00 52 35.47	-72 50 49.9	4.11 ± 0.04	3.85 ± 0.34	4.05 ± 0.21	1.32	0.91	e	—
79978	01 20 47.90	-73 36 25.1	4.11 ± 0.03	3.65 ± 0.14	3.41 ± 0.31	1.18	0.72	e	—
75962	01 15 13.73	-73 20 03.2	4.45 ± 0.01	3.68 ± 0.07	4.86 ± 0.21	1.27	1.24	e	—
77607	01 17 17.96	-73 24 52.1	4.15 ± 0.03	3.18 ± 0.15	3.02 ± 0.3	0.93	—	e	—
81634	01 24 50.25	-73 34 12.7	4.15 ± 0.05	3.88 ± 0.32	4.12 ± 0.25	1.34	0.93	e	—
57397	01 03 47.54	-72 12 58.6	4.23 ± 0.06	4.51 ± 0.42	4.2 ± 0.24	—	—	e	—
49517	01 00 42.30	-72 37 26.6	4.2 ± 0.08	4.51 ± 0.5	4.12 ± 0.25	—	0.93	e	—
80277	01 21 30.75	-73 29 02.4	4.15 ± 0.03	3.48 ± 0.14	3.16 ± 0.24	1.1	—	e	—
298	00 40 43.96	-73 24 22.8	4.11 ± 0.03	3.75 ± 0.21	3.94 ± 0.25	1.27	0.87	e	—
83010	01 28 46.17	-73 17 42.0	4.11 ± 0.04	3.45 ± 0.21	0.0 ± 0.0	1.07	—	e	—
80684	01 22 33.87	-73 18 21.3	4.08 ± 0.03	3.81 ± 0.29	3.43 ± 0.25	1.3	0.72	e	—
1952	00 42 31.91	-73 22 00.9	4.08 ± 0.03	4.21 ± 0.1	3.76 ± 0.25	1.66	0.82	e	m
75994	01 15 15.27	-73 05 59.3	4.08 ± 0.04	3.61 ± 0.16	3.39 ± 0.19	1.16	0.71	e	—
30472	00 54 33.08	-72 12 53.9	4.08 ± 0.02	3.81 ± 0.17	3.76 ± 0.24	1.3	0.82	e	m
77388	01 16 58.68	-73 07 07.1	4.11 ± 0.03	3.65 ± 0.13	3.41 ± 0.21	1.18	0.72	e	—
82078	01 25 55.88	-73 13 49.3	4.11 ± 0.04	3.65 ± 0.13	3.45 ± 0.31	1.18	0.73	e	—
83483	01 30 11.44	-73 20 36.5	4.11 ± 0.05	3.65 ± 0.22	0.0 ± 0.0	1.18	—	e	—
81348	01 24 11.58	-73 14 28.4	4.11 ± 0.04	3.85 ± 0.15	4.17 ± 0.24	1.32	0.95	e	—
73701	01 12 47.67	-73 14 43.2	4.11 ± 0.03	3.55 ± 0.16	3.41 ± 0.31	1.12	0.72	e	—
73256	01 12 24.21	-73 14 33.3	4.11 ± 0.04	3.75 ± 0.17	2.97 ± 0.31	1.27	—	e	—
6940	00 46 23.76	-73 02 24.0	4.08 ± 0.02	3.71 ± 0.12	3.95 ± 0.19	1.22	0.88	e	—
80579	01 22 15.34	-73 14 00.4	4.11 ± 0.03	3.85 ± 0.13	3.92 ± 0.24	1.32	0.87	—	—

Table 1 continued

Table 1 (*continued*)

M2002 ID	RA (J2000)	Dec (J2000)	$\log T_{\text{eff}}$	$\log \mathcal{L}$	$\log L$	$\log M_{\text{sHRD}}$	$\log M_{\text{HRD}}$	Oe/Be	Metals
	[h, m, s]	[$^{\circ}, ^{\prime}, ^{\prime\prime}$]	[K]	[\mathcal{L}_{\odot}]	[L_{\odot}]	[M_{\odot}]	[M_{\odot}]		
80412	01 21 49.54	-73 37 21.5	4.08 ± 0.05	3.71 ± 0.41	4.31 ± 0.24	1.22	1.0	e	m
75984	01 15 14.76	-72 20 19.6	4.11 ± 0.0	3.85 ± 0.02	3.84 ± 0.24	1.32	0.85	e	-
27135	00 53 30.90	-73 03 07.5	4.08 ± 0.04	4.11 ± 0.29	3.65 ± 0.3	1.57	0.78	e	-
23859	00 52 33.80	-72 16 59.9	4.08 ± 0.03	3.71 ± 0.18	3.83 ± 0.25	1.22	0.84	e	-
64710	01 06 49.07	-71 59 00.7	4.08 ± 0.03	3.81 ± 0.13	3.97 ± 0.24	1.3	0.88	e	-
83224	01 29 22.81	-73 15 56.4	4.11 ± 0.05	4.45 ± 0.52	4.05 ± 0.24	-	0.91	e	-
45640	00 59 12.70	-71 38 44.8	4.11 ± 0.02	3.85 ± 0.16	4.24 ± 0.25	1.32	-	e	-
80573	01 22 14.57	-73 08 25.2	4.11 ± 0.03	4.05 ± 0.11	4.07 ± 0.24	1.5	0.92	-	-
81465	01 24 27.82	-73 32 57.2	4.08 ± 0.04	3.91 ± 0.37	3.89 ± 0.24	1.4	0.86	e	-
77223	01 16 44.80	-73 18 27.7	4.08 ± 0.09	3.91 ± 0.38	3.31 ± 0.19	1.4	0.7	e	-
77025	01 16 28.06	-73 17 20.1	4.08 ± 0.05	3.81 ± 0.27	0.0 ± 0.0	1.3	-	e	-
81671	01 24 54.49	-73 09 11.4	4.08 ± 0.03	3.71 ± 0.09	3.56 ± 0.31	1.22	0.76	e	-
18329	00 50 59.47	-73 32 03.8	4.08 ± 0.03	3.71 ± 0.19	4.01 ± 0.3	1.22	0.9	e	-
38921	00 57 00.75	-72 08 10.9	4.08 ± 0.03	3.21 ± 0.14	4.13 ± 0.19	0.94	0.93	e	-
80960	01 23 14.34	-73 08 57.7	4.08 ± 0.01	2.71 ± 0.13	3.27 ± 0.32	0.72	-	-	-
61842	01 05 24.73	-73 03 52.8	4.04 ± 0.02	3.96 ± 0.13	4.31 ± 0.19	1.39	1.0	e	-
32752	00 55 12.66	-73 26 52.5	4.04 ± 0.02	3.96 ± 0.24	4.0 ± 0.31	1.39	0.89	e	-
79697	01 20 18.09	-72 18 53.7	4.08 ± 0.01	3.91 ± 0.11	3.85 ± 0.24	1.4	0.85	e	-
36975	00 56 24.66	-73 16 45.9	4.04 ± 0.01	4.06 ± 0.1	3.72 ± 0.3	1.52	0.8	e	-
50396	01 01 04.58	-72 20 23.6	4.04 ± 0.03	4.06 ± 0.23	3.65 ± 0.21	1.52	0.78	e	-
51214	01 01 25.44	-71 46 40.3	4.0 ± 0.04	3.79 ± 0.24	3.71 ± 0.21	1.27	0.8	e	-
83480	01 30 10.89	-73 18 56.2	4.04 ± 0.04	4.06 ± 0.4	4.3 ± 0.24	1.52	1.0	e	-
82019	01 25 47.79	-73 08 39.0	4.0 ± 0.01	3.09 ± 0.07	3.39 ± 0.31	0.89	0.71	-	-

NOTE— Columns 1, 2 and 3: identification and coordinates from [Massey \(2002\)](#). Cols. 4, 5 and 6: effective temperature, spectroscopic luminosity and luminosity obtained in this work. Column 7 and 8 present the masses estimated in the sHRD and HRD respectively. Stars with emissions in any of the Balmer lines are labeled with 'e' in column 9. Stars with Si III $\lambda 4552$ equivalent width larger than 0.15 Å are labeled with 'm' in column 10. The spectral classification can be seen in [Evans et al. \(2004\)](#) and [Lamb et al. \(2016\)](#). Table 1 is also available in machine-readable format.

This work was supported by NSF grant AST-1514838 to MSO and by the University of Michigan.

Software: FASTWIND ([Santolaya-Rey et al. 1997](#); [Puls et al. 2005](#)), Astropy ([Astropy Collaboration et al. 2013](#)), APIpy ([Robitaille & Bressert 2012](#)) and COSMOS pipeline ([Dressler et al. 2011](#); [Oemler et al. 2017](#)).

REFERENCES

- Abbott, B. P., Abbott, R., Abbott, T. D., et al. 2017, Phys. Rev. Lett., 118, 221101,
doi: [10.1103/PhysRevLett.118.221101](https://doi.org/10.1103/PhysRevLett.118.221101)
- Astropy Collaboration, Robitaille, T. P., Tollerud, E. J., et al. 2013, A&A, 558, A33,
doi: [10.1051/0004-6361/201322068](https://doi.org/10.1051/0004-6361/201322068)

- Bigelow, B. C., & Dressler, A. M. 2003, in Proc. SPIE, Vol. 4841, Instrument Design and Performance for Optical/Infrared Ground-based Telescopes, ed. M. Iye & A. F. M. Moorwood, 1727–1738
- Bonanos, A. Z., Lennon, D. J., Köhlinger, F., et al. 2010, AJ, 140, 416, doi: [10.1088/0004-6256/140/2/416](https://doi.org/10.1088/0004-6256/140/2/416)
- Brott, I., de Mink, S. E., Cantiello, M., et al. 2011, A&A, 530, A115, doi: [10.1051/0004-6361/201016113](https://doi.org/10.1051/0004-6361/201016113)
- Castro, N., Fossati, L., Langer, N., et al. 2014, A&A, 570, L13, doi: [10.1051/0004-6361/201425028](https://doi.org/10.1051/0004-6361/201425028)
- Castro, N., Urbaneja, M. A., Herrero, A., et al. 2012, A&A, 542, A79, doi: [10.1051/0004-6361/201118253](https://doi.org/10.1051/0004-6361/201118253)
- Ceverino, D., & Klypin, A. 2009, ApJ, 695, 292, doi: [10.1088/0004-637X/695/1/292](https://doi.org/10.1088/0004-637X/695/1/292)
- Dias, B., Kerber, L., Barbuy, B., Bica, E., & Ortolani, S. 2016, A&A, 591, A11, doi: [10.1051/0004-6361/201527558](https://doi.org/10.1051/0004-6361/201527558)
- Dobbie, P. D., Cole, A. A., Subramaniam, A., & Keller, S. 2014, MNRAS, 442, 1680, doi: [10.1093/mnras/stu926](https://doi.org/10.1093/mnras/stu926)
- Doom, C. 1985, A&A, 142, 143
- Dressler, A., Bigelow, B., Hare, T., et al. 2011, Publications of the Astronomical Society of the Pacific, 123, 288, doi: [10.1086/658908](https://doi.org/10.1086/658908)
- Ekström, S., Georgy, C., Eggenberger, P., et al. 2012, A&A, 537, A146, doi: [10.1051/0004-6361/201117751](https://doi.org/10.1051/0004-6361/201117751)
- Evans, C., Taylor, W., Sana, H., et al. 2011, The Messenger, 145, 33
- Evans, C. J., Bresolin, F., Urbaneja, M. A., et al. 2007, ApJ, 659, 1198, doi: [10.1086/511382](https://doi.org/10.1086/511382)
- Evans, C. J., Howarth, I. D., Irwin, M. J., Burnley, A. W., & Harries, T. J. 2004, MNRAS, 353, 601, doi: [10.1111/j.1365-2966.2004.08096.x](https://doi.org/10.1111/j.1365-2966.2004.08096.x)
- Fitzpatrick, E. L., & Garmany, C. D. 1990, ApJ, 363, 119, doi: [10.1086/169322](https://doi.org/10.1086/169322)
- Garcia, M., Herrero, A., Najarro, F., Lennon, D. J., & Alejandro Urbaneja, M. 2014, ApJ, 788, 64, doi: [10.1088/0004-637X/788/1/64](https://doi.org/10.1088/0004-637X/788/1/64)
- Georgy, C., Ekström, S., Eggenberger, P., et al. 2013, A&A, 558, A103, doi: [10.1051/0004-6361/201322178](https://doi.org/10.1051/0004-6361/201322178)
- Golden-Marx, J. B., Oey, M. S., Lamb, J. B., Graus, A. S., & White, A. S. 2016, ApJ, 819, 55, doi: [10.3847/0004-637X/819/1/55](https://doi.org/10.3847/0004-637X/819/1/55)
- Gordon, K. D., Clayton, G. C., Misselt, K. A., Landolt, A. U., & Wolff, M. J. 2003, ApJ, 594, 279, doi: [10.1086/376774](https://doi.org/10.1086/376774)
- Graczyk, D., Pietrzynski, G., Thompson, I. B., et al. 2014, ApJ, 780, 59, doi: [10.1088/0004-637X/780/1/59](https://doi.org/10.1088/0004-637X/780/1/59)
- Haiman, Z., & Loeb, A. 1997, ApJ, 483, 21, doi: [10.1086/304238](https://doi.org/10.1086/304238)
- Herrero, A., Kudritzki, R. P., Vilchez, J. M., et al. 1992, A&A, 261, 209
- Holgado, G., Simón-Díaz, S., Barbá, R. H., et al. 2017, ArXiv e-prints. <https://arxiv.org/abs/1711.10043>
- Jokuthy, A. 2002, PhD thesis, Diploma thesis, University Munich
- Kennicutt, R. C., & Evans, N. J. 2012, ARA&A, 50, 531, doi: [10.1146/annurev-astro-081811-125610](https://doi.org/10.1146/annurev-astro-081811-125610)
- Kudritzki, R.-P., & Puls, J. 2000, ARA&A, 38, 613, doi: [10.1146/annurev.astro.38.1.613](https://doi.org/10.1146/annurev.astro.38.1.613)
- Lamb, J. B., Oey, M. S., Segura-Cox, D. M., et al. 2016, ApJ, 817, 113, doi: [10.3847/0004-637X/817/2/113](https://doi.org/10.3847/0004-637X/817/2/113)
- Langer, N. 2012, ARA&A, 50, 107, doi: [10.1146/annurev-astro-081811-125534](https://doi.org/10.1146/annurev-astro-081811-125534)
- Langer, N., & Kudritzki, R. P. 2014, A&A, 564, A52, doi: [10.1051/0004-6361/201423374](https://doi.org/10.1051/0004-6361/201423374)
- Larsen, S. S., de Mink, S. E., Eldridge, J. J., et al. 2011, A&A, 532, A147, doi: [10.1051/0004-6361/201117185](https://doi.org/10.1051/0004-6361/201117185)
- Lefever, K., Puls, J., Morel, T., et al. 2010, A&A, 515, A74, doi: [10.1051/0004-6361/200911956](https://doi.org/10.1051/0004-6361/200911956)
- Lennon, D. J., Dufton, P. L., & Fitzsimmons, A. 1993, A&AS, 97, 559
- Marchant, P., Langer, N., Podsiadlowski, P., Tauris, T. M., & Moriya, T. J. 2016, A&A, 588, A50, doi: [10.1051/0004-6361/201628133](https://doi.org/10.1051/0004-6361/201628133)
- Markova, N., & Puls, J. 2015, in IAU Symposium, Vol. 307, New Windows on Massive Stars, ed. G. Meynet, C. Georgy, J. Groh, & P. Stee, 117–118
- Markova, N., Puls, J., & Langer, N. 2018, ArXiv e-prints. <https://arxiv.org/abs/1803.03410>
- Martins, F., & Palacios, A. 2017, A&A, 598, A56, doi: [10.1051/0004-6361/201629538](https://doi.org/10.1051/0004-6361/201629538)
- Massey, P. 2002, ApJS, 141, 81, doi: [10.1086/338286](https://doi.org/10.1086/338286)
- McErlean, N. D., Lennon, D. J., & Dufton, P. L. 1999, A&A, 349, 553
- Moe, M., & Di Stefano, R. 2017, The Astrophysical Journal Supplement Series, 230, 15, doi: [10.3847/1538-4365/aa6fb6](https://doi.org/10.3847/1538-4365/aa6fb6)
- Mokiem, M. R., de Koter, A., Evans, C. J., et al. 2006, A&A, 456, 1131, doi: [10.1051/0004-6361:20064995](https://doi.org/10.1051/0004-6361:20064995)
- Morel, T., Castro, N., Fossati, L., et al. 2014, The Messenger, 157, 27
- Nieva, M.-F., & Przybilla, N. 2012, A&A, 539, A143, doi: [10.1051/0004-6361/201118158](https://doi.org/10.1051/0004-6361/201118158)
- Oemler, A., Clardy, K., Kelson, D., Walth, G., & Villanueva, E. 2017, COSMOS: Carnegie Observatories System for MultiObject Spectroscopy, Astrophysics Source Code Library. <http://ascl.net/1705.001>
- Oey, M. S., King, N. L., & Parker, J. W. 2004, AJ, 127, 1632, doi: [10.1086/381926](https://doi.org/10.1086/381926)
- Poelarends, A. J. T., Herwig, F., Langer, N., & Heger, A. 2008, ApJ, 675, 614, doi: [10.1086/520872](https://doi.org/10.1086/520872)

- Puls, J., Urbaneja, M. A., Venero, R., et al. 2005, *A&A*, 435, 669, doi: [10.1051/0004-6361:20042365](https://doi.org/10.1051/0004-6361:20042365)
- Puls, J., Kudritzki, R.-P., Herrero, A., et al. 1996, *A&A*, 305, 171
- Ramírez-Agudelo, O. H., Sana, H., de Koter, A., et al. 2017, *A&A*, 600, A81, doi: [10.1051/0004-6361/201628914](https://doi.org/10.1051/0004-6361/201628914)
- Ripepi, V., Cioni, M.-R. L., Moretti, M. I., et al. 2017, *MNRAS*, 472, 808, doi: [10.1093/mnras/stx2096](https://doi.org/10.1093/mnras/stx2096)
- Rivero González, J. G., Puls, J., Massey, P., & Najarro, F. 2012, *A&A*, 543, A95, doi: [10.1051/0004-6361/201218955](https://doi.org/10.1051/0004-6361/201218955)
- Rivinius, T., Carciofi, A. C., & Martayan, C. 2013, *A&A Rv*, 21, 69, doi: [10.1007/s00159-013-0069-0](https://doi.org/10.1007/s00159-013-0069-0)
- Robitaille, T., & Bressert, E. 2012, APLpy: Astronomical Plotting Library in Python, Astrophysics Source Code Library. <http://ascl.net/1208.017>
- Sabín-Sanjulián, C., Simón-Díaz, S., Herrero, A., et al. 2017, *A&A*, 601, A79, doi: [10.1051/0004-6361/201629210](https://doi.org/10.1051/0004-6361/201629210)
- Sana, H., de Mink, S. E., de Koter, A., et al. 2012, *Science*, 337, 444, doi: [10.1126/science.1223344](https://doi.org/10.1126/science.1223344)
- Santolaya-Rey, A. E., Puls, J., & Herrero, A. 1997, *A&A*, 323, 488
- Sanyal, D., Grassitelli, L., Langer, N., & Bestenlehner, J. M. 2015, *A&A*, 580, A20, doi: [10.1051/0004-6361/201525945](https://doi.org/10.1051/0004-6361/201525945)
- Sanyal, D., Langer, N., Szécsi, D., -C Yoon, S., & Grassitelli, L. 2017, *A&A*, 597, A71, doi: [10.1051/0004-6361/201629612](https://doi.org/10.1051/0004-6361/201629612)
- Schneider, F. R. N., Castro, N., Fossati, L., Langer, N., & de Koter, A. 2017, *A&A*, 598, A60, doi: [10.1051/0004-6361/201628409](https://doi.org/10.1051/0004-6361/201628409)
- Schneider, F. R. N., Sana, H., Evans, C. J., et al. 2018, *Science*, 359, 69, doi: [10.1126/science.aan0106](https://doi.org/10.1126/science.aan0106)
- Scowcroft, V., Freedman, W. L., Madore, B. F., et al. 2016, *ApJ*, 816, 49, doi: [10.3847/0004-637X/816/2/49](https://doi.org/10.3847/0004-637X/816/2/49)
- Simón-Díaz, S., Godart, M., Castro, N., et al. 2017, *A&A*, 597, A22, doi: [10.1051/0004-6361/201628541](https://doi.org/10.1051/0004-6361/201628541)
- Smith, R. C., & MCELS Team. 1998, *PASA*, 15, 163, doi: [10.1071/AS98163](https://doi.org/10.1071/AS98163)
- Trundle, C., Dufton, P. L., Hunter, I., et al. 2007, *A&A*, 471, 625, doi: [10.1051/0004-6361:20077838](https://doi.org/10.1051/0004-6361:20077838)
- Urbaneja, M. A., Herrero, A., Bresolin, F., et al. 2005, *ApJ*, 622, 862, doi: [10.1086/427468](https://doi.org/10.1086/427468)
- Vink, J. S., Brott, I., Gräfener, G., et al. 2010, *A&A*, 512, L7, doi: [10.1051/0004-6361/201014205](https://doi.org/10.1051/0004-6361/201014205)
- Vink, J. S., Heger, A., Krumholz, M. R., et al. 2015, *Highlights of Astronomy*, 16, 51, doi: [10.1017/S1743921314004657](https://doi.org/10.1017/S1743921314004657)
- Wade, G. A., Grunhut, J., Alecian, E., et al. 2014, in IAU Symposium, Vol. 302, Magnetic Fields throughout Stellar Evolution, ed. P. Petit, M. Jardine, & H. C. Spruit, 265–269
- Weidner, C., & Vink, J. S. 2010, *A&A*, 524, A98, doi: [10.1051/0004-6361/201014491](https://doi.org/10.1051/0004-6361/201014491)
- Woosley, S. E., & Bloom, J. S. 2006, *ARA&A*, 44, 507, doi: [10.1146/annurev.astro.43.072103.150558](https://doi.org/10.1146/annurev.astro.43.072103.150558)
- Yorke, H. W. 1986, *Annual Review of Astronomy and Astrophysics*, 24, 49, doi: [10.1146/annurev.aa.24.090186.000405](https://doi.org/10.1146/annurev.aa.24.090186.000405)